Journal of Mathematical Imaging and Vision (2019) 61:885–917
https://doi.org/10.1007/s10851-019-00876-1

Nonparametric Blind Super-Resolution Using Adaptive Heavy-Tailed Priors

Wen-Ze Shao[1,2] · Qi Ge[1] · Li-Qian Wang[1] · Yun-Zhi Lin[3,4] · Hai-Song Deng[5] · Hai-Bo Li[6,1]

Received: 19 June 2018 / Accepted: 15 February 2019 / Published online: 27 February 2019

Abstract

Single-image nonparametric blind super-resolution is a fundamental image restoration problem yet largely ignored in the past decades among the computational photography and computer vision communities. An interesting phenomenon is observed that learning-based single-image super-resolution (SR) has been experiencing a rapid development since the boom of the sparse representation in 2005s and especially the representation learning in 2010s, wherein the high-res image is generally blurred by a supposed bicubic or Gaussian blur kernel. However, the parametric assumption on the form of blur kernels does not hold in most practical applications because in real low-res imaging a high-res image can undergo complex blur processes, e.g., Gaussian-shaped kernels of varying sizes, ellipse-shaped kernels of varying orientations, curvilinear kernels of varying trajectories. The paper is mainly motivated by one of our previous works: Shao and Elad (in: Zhang (ed) ICIG 2015, Part III, Lecture notes in computer science, Springer, Cham, 2015). Specifically, we take one step further in this paper and present a type of adaptive heavy-tailed image priors, which result in a new regularized formulation for nonparametric blind super-resolution. The new image priors can be expressed and understood as a generalized integration of the normalized sparsity measure and relative total variation. Although it seems that the proposed priors are simple, the core merit of the priors is their practical capability for the challenging task of nonparametric blur kernel estimation for both super-resolution and deblurring. Harnessing the priors, a higher-quality intermediate high-res image becomes possible and therefore more accurate blur kernel estimation can be accomplished. A great many experiments are performed on both synthetic and real-world blurred low-res images, demonstrating the comparative or even superior performance of the proposed algorithm convincingly. Meanwhile, the proposed priors are demonstrated quite applicable to blind image deblurring which is a degenerated problem of nonparametric blind SR.

Keywords Super-resolution · Blind deconvolution · Camera shake deblurring · Discriminative models · Convolutional neural networks · Normalized sparsity · Relative total variation

1 Introduction

As a fundamental image restoration problem, single-frame super-resolution (SISR) has undergone a rapid development since the pioneering work by Freeman and Pasztor [1] and Baker and Kanade [2]. Several comprehensive surveys [3–6] provide detailed elaborations, comparisons and comments on the super-resolution algorithms up to 2013, wherein it is noted clearly that the learning-based strategies manifest more and more potentials in terms of both accuracy and efficiency, as compared against the popular variational methods in the scenario of multi-frame super-resolution. In the recent few years, single-frame super-resolution has experienced another round of boom [82–84] because of the strong return of modern neural networks, i.e., deep learning [7–10,

✉ Wen-Ze Shao
shaowenze1010@163.com

[1] College of Telecommunications and Information Engineering, Nanjing University of Posts and Telecommunications (NUPT), Nanjing, China

[2] National Engineering Research Center of Communications and Networking, NUPT, Nanjing, China

[3] School of Electrical and Computer Engineering, Georgia Institute of Technology, Atlanta, Georgia

[4] School of Automation, Southeast University, Nanjing, China

[5] School of Science, Nanjing Audit University, Nanjing, China

[6] School of Computer Science and Communication, KTH Royal Institute of Technology, Stockholm, Sweden

27–37, 78, 80, 81], achieving convincing and sometimes amazing performance in terms of both objective and subjective assessments.

1.1 Learning-Based SISR

The basic idea of learning-based SISR approaches is to learn a single or multiple mappings between the low-res (LR) and high-res (HR) domains by harnessing a large set of training image pairs, where every HR training image is blurred by a supposed bicubic or Gaussian blur kernel. To make clear the motivation in the present paper, a short review on the representative learning-based SISR approaches is provided, which essentially originate from three kinds of machine learning methodologies, i.e., manifold learning, sparse learning and deep learning, based on which four types of SISR algorithms are summarized in the following.

Neighborhood embedding Two representative SISR approaches of this type are [11, 12], supposing that patches of an LR image and its HR counterpart form manifolds with similar local geometric characteristics in two distinct feature spaces, roughly implying that as long as enough sampled patches are available, patches in the HR feature space can be recovered as a weighted average of local neighbors using the same weights as ones in the HR feature space, where the estimation of weights may be formulated into a constrained least squares problem. One may refer to [13, 14] for recent advancements in this branch.

Coupled dictionary learning Two representative SISR methods of this type are [15, 16], whose core idea is to learn coupled dictionaries for the LR and HR image patches while forcing exactly the same sparse coding coefficients in the two domains. Then, a test HR patch can be reconstructed by using the sparse coding coefficients of its counterpart LR patch and the pre-learned HR dictionary. The idea initially originated from Yang et al. [15] later improved in Zeyde et al. [16] for both accuracy and speed. Furthermore, semi-coupled dictionary learning methods [17–23, 79] are proposed recently, aiming to relax the same sparse coding assumption while at the cost of more computational burden.

Locally linear regression Inspired by the above learning principles, several models emerge proposing to replace the time-consuming sparse coding by locally linear regression. Two representative algorithms in this type are [24, 25]. For instance, instead of building on the L_1-norm-based sparse representation as in [15, 16], ANR (anchored neighborhood regression) [24] formulates a SISR mapping into multiple linear operators, which are pre-computed using the clustered atoms (termed "anchor neighbors") so as to obtain an overall switched linear mapping from LR to HR images. Later, A+ [25] improves [24] in a straightforward manner with clustered training patches as anchor neighbors. Except for [24, 25], a novel locality idea is also established in [26] via a hierarchical structure in a random forest.

Convolutional neural networks Much more recently, extraordinary success achieved by deep learning in computer vision inspires the use of convolutional neural networks (CNN) with deep architecture for SISR [27, 28]. For instance, multi-layers of collaborative autoencoders are stacked together in [27] for robust matching of self-similar patches. A deep CNN is trained in [28] to directly learn a nonlinear mapping from LR to HR domains in a similar principle to coupled dictionary learning [15, 16]. As extensions to [27, 28], several more advanced deep architectures have been developed for better SISR, such as very deep CNN [29], deeply recursive CNN [30], perception-induced CNN [31] and so on [32–37]. Currently, the CNN-based methodologies become the absolute mainstream for SISR and are also successfully applied to the specific face hallucination problem [38, 39, 78].

1.2 Nonparametric Blind SISR

Though SISR has earned intensive attention in the past two decades, a careful inspection reveals that there exists a common assumption in the current literature, namely, the high-res image is blurred by a supposed bicubic or Gaussian blur kernel with a known standard deviation. And actually, most of existing learning-based approaches use the bicubic low-pass filter (implemented via MATLAB's default function *imresize*) to generate the LR-HR training pairs. We note that the parametric assumption on the form of blur kernels apparently does not hold in most practical applications, that is because an HR image can undergo complicated blur processes in real low-res imaging, e.g., Gaussian-shaped kernels of varying sizes, ellipse-shaped kernels of varying orientations, curvilinear kernels of varying trajectories. This largely ignored problem not only exists in the current learning-based methods but also the classic reconstruction-based approaches such as [40–42]. Indeed, advanced image models, either the learning-based or the variational ones, are important to the final SISR quality. However, an interesting critical study by Efrat et al. [43] demonstrates that, for a general SISR problem, the influence of an accurate blur kernel is significantly larger than that of an advanced image model. What is more surprising as phrased that, "an accurate reconstruction constraint (i.e., knowing the blur kernel) combined with a simple gradient regularization achieves super-resolution results almost as good as those of state-of-the-art algorithms with sophisticated image priors." Hence, as super-resolving a real blurry low-res image, precise and robust estimation of nonparametric blur kernels should be considered the first most important thing, without which the final high-res image would manifest either ringing or blurring artifacts as demonstrated in [43].

According to intensive literature review, only few works have addressed estimating an accurate blur kernel in the scenario of SISR. Among few such works a parametric model is often assumed, and the Gaussian is a common choice, e.g., [44–46]. However, as the assumption does not coincide with the actual blur model, e.g., combination of out-of-focus and camera shake, we will naturally get low-quality SR results. To the best of our knowledge, the first daring attempt toward nonparametric blur kernel estimation for single-image SR is made in [47] and its problem solution also applies to blind image deblurring. However, it restricts its treatment to single-peak blur kernels and does not originate from a rigorous optimization principle but relies on empirical detection and prediction of step edges as important clues to blur kernel estimation. A second noteworthy work for nonparametric blind SR is the one by Michaeli and Irani [48] whose essential idea is to harness the recurrence property of natural image patches across different scales. It should be noted that the performance of this approach relies heavily on the searched nearest neighbors to the query patches in the input blurry low-res image. Besides, as claimed in [49], the modeling idea in [48] cannot be naively applicable to the blind deblurring task [85–89]. Taking into account the similarity between blind deblurring and blind super-resolution in terms of nonparametric blur kernel estimation, the first author of the present paper and his collaborator recently propose to formulate both blind problems in a common modeling perspective [50], i.e., bi-L_0–L_2-norm regularization [51]. In spite of that the endeavor being made in [50] is preliminary, it really brings us an enlightenment that the gap between two blind restoration problems can be narrowed to a certain degree. Indeed, the attention given to the nonparametric blind SR is rather limited, but the counterpart blind deblurring has been intensively studied since the seminal work of Fergus et al. on camera shake removal [52]. Thus, a natural possibility is to extend existing blind deblurring models to the blind SR task in a framework similar as that of [50]. Very recently, Lai et al. [53] conduct a systematically comparative study on state-of-the-art blind deblurring algorithms which were published during 2006–2015. They reveal a cruel fact that the performance of these methods is generally found inferior on real-blurred images to that on one or another synthetic benchmark dataset. That is, blind deblurring models at hand are far from being practical in terms of the final deblurring quality. We notice that an interesting breakthrough is just made by Pan et al. [54, 87]. They impose an L_0-norm-based prior in both image gradient and dark channel domains, leading to advanced state-of-the-art performance in various kinds of imaging scenarios, e.g., natural, manmade, low-illumination, text and face images. However, on the one hand, the L_0-norm-based prior in Pan et al. [54] is not discriminative as a whole just similar to the blind models in Lai et al. [53]; on the other hand, their numerical algorithm is computationally expensive which is another major concern as developing blind SR methods. Very recently, Pan et al. [55] extend their L_0-norm-based blind model [56] defined in both image gradient and intensity domains to the blind SR problem, which largely resembles that of ours in [50]. However, nonparametric blind SR with an image prior in either [56] or [54] will bear a much higher computational burden, and hence in terms of the numerical efficiency, either Pan et al. [54] or Pan et al. [56] is not a feasible and effective candidate to blind SR.

1.3 Contributions in This Paper

In this paper, we build on our preliminary work in [50] while taking a step further. Specifically, we develop a novel ADMM method for nonparametric blind SR by proposing a type of L_α-norm-based adaptive heavy-tailed image priors, to some extent, which can be expressed and understood as a generalized integration of the previous normalized sparsity measure [67] and relative total variation [72]. Combining the adaptive priors and convolutional consistency constraint (CCC) as advocated in [50], a higher-quality intermediate high-res image becomes possible and, hence, more accurate blur kernel estimation can be achieved for nonparametric blind SR. As for minimization of the resulting functional, an ADMM-based iterative algorithm is derived for estimating the intermediate high-res image and nonparametric blur kernel alternatingly, during which the conjugate gradient algorithm is exploited for running efficiency. A great many experiments are performed on both synthetic and real-world blurry low-res images, demonstrating the comparative or even superior performance of the proposed method convincingly. An empirical study is also made toward appropriate choice of existing SISR algorithms for the convolutional consistency constraint. The candidates come from previously introduced four categories of learning-based methods, i.e., *neighborhood embedding*, *coupled dictionary learning, locally linear regression, convolutional neural networks*, considering their potential advantages in terms of both accuracy and efficiency. It is not surprising that the empirical observation conforms to that in [50], i.e., ANR (anchored neighborhood regression) [24] is demonstrated the more robust engine for our purpose than other candidates including the advanced deep learning-based methodology. In the meantime, the proposed adaptive priors are also applied to the degenerated task of nonparametric blind SR, i.e., blind deblurring. The new priors are demonstrated fit the blind deblurring problem as well.

It seems that the mathematical novelty of the proposed approach is not that sufficient considering the new priors is actually a combination of two off-the-shelf ones, i.e., [67, 72]. Nevertheless, we believe that the core merit of the new priors is their practical capability for the challenging task of nonparametric blur kernel estimation for both super-resolution and deblurring. In the below, we have made further explanations on the motivation and highlight of the proposed method.

(1) First of all, in the literature very few works have addressed accurate blur kernel estimation toward the problem of nonparametric blind super-resolution. The difficulty lies in that, on the one hand, there has lacked an effective modeling framework for the problem for a long time until the emergence of several recent references, e.g., [47, 48, 50]. Thus, we make one step further in this paper trying to improve our previous work [50] with the proposal of a kind of more effective image priors for nonparametric blur kernel estimation. On the other hand, this paper is still motivated by the expectation that a really good image model for nonparametric blind super-resolution has to be also more effective to nonparametric blind deblurring. The reason is that nonparametric blind deblurring is apparently a degenerated task of nonparametric blind super-resolution. However, the blind deblurring results in Sect. 4.3 of this paper reveal that the bi-L_0–L_2-norm regularization in [50] is obviously not comparative to the proposed heavy-tailed priors, in terms of both estimation precision and robustness. Hence, it is believed that the core contribution of this paper is not trivial at least in the unified modeling point of view for practice. As for the nonparametric blind method [47], it restricts its treatment to single-peak blur kernels and builds on empirical detection and prediction of step edges as critical clues to blur kernel estimation, while, as for the method in [48] for nonparametric blind SR, its proposed model cannot be applicable to blind deblurring as validated in [49].

(2) On the second, the present paper tries to address nonparametric blur kernel estimation for both super-resolution and image deblurring in a simpler modeling perspective, which is purely gradient-based and therefore allows us to derive a flexible numerical optimization scheme in the variational framework. To achieve the goal, a new type of spatially adaptive weights tailored specifically for blur kernel estimation is proposed and just embedded into the existing hyper-Laplacian priors. Indeed, as pointed out by one of the reviewers, in the literature there exist related works using local weights in both convex and non-convex gradient penalties. Such weighted schemes are also very popular among the signal and image processing community, e.g., [95, 96]. However, it is really non-trivial to make such a contribution practically work for both blind restoration problems, despite that the critical components in the proposed adaptive weights are the off-the-shelf ones, i.e., normalized sparsity measure and relative total variation. For one thing, although the normalized sparsity measure [67] is the first discriminative regularization specifically exploited for nonparametric blur kernel estimation, its practical performance is quite limited according to the experimental results on both synthetic and real-world data in recent two studies [53, 54]. For another, this work reveals an interesting and instructive fact that the principle of discriminativeness between a sharp image and its blurry counterpart in the image prior is not the solely essential element for nonparametric blind restoration; a really good image prior for the problem should be also capable of discriminating between the strong edge and weak texture structures. What makes us particularly surprised is that such double principles of discriminativeness (DPD) are simply implemented via re-weighting the known gradient-based hyper-Laplacian priors. To the best of our knowledge, it is the first time that the concept of DPD is clarified for the nonparametric blind restoration problems. Apparently, those L_0-norm-based priors [51, 54, 56, 87] including the bi-L_0–L_2-norm regularization do not satisfy DPD as a whole. Besides, [54, 56, 87] have essentially formulated image priors in both the gradient and intensity domains and therefore are not conceptually simple and numerically efficient. The comparison on the running efficiency among the proposed priors and those of [54, 56] for blind deblurring is additionally made in Sect. 4.3 of this paper as suggested by one of the reviewers.

We organize the rest part of the paper as follows. Section 2 provides a short review on L_α-norm-based image priors and their applications in image processing and computational imaging, based on which the proposed adaptive heavy-tailed priors are presented, elaborated and harnessed to regularize the nonparametric blind SR problem. In Sect. 3, the ADMM-based numerical algorithm is deduced for alternatingly iterative update of the intermediate high-res image and nonparametric blur kernel, with possible implementation details clarified. Section 4 analyzes the proposed blind SR approach on both synthetic and realistic blurred low-res images, along with comparisons against Michaeli and Irani [48] and our previous work [50]. Additionally, the applicability of our new priors to blind deblurring is tested in this section. The paper is finally concluded in Sect. 5.

2 Nonparametric Blind Super-Resolution Using Adaptive Heavy-Tailed Image Priors

2.1 L_α-Norm-Based Heavy-Tailed Priors for Image Restoration: A Brief Review

For the sake of better understanding the proposed method in this paper, several previous works using L_α-norm-based heavy-tailed priors are introduced in this subsection. Without loss of generality, the heavy-tailed distribution of image gradients termed hyper-Laplacian priors [62] is given as $p(u) \propto \prod_{p\in\Omega} \exp\{-\gamma(|\partial_x u_p|^\alpha + |\partial_y u_p|^\alpha)\}$, where $p \in \Omega$ denotes a pixel index in the image region Ω, $0 < \alpha \le 1$ amounts to imposing the L_α-norm-based regularization on the image gradients, and γ is a positive tuning parameter controlling the strength of regularization, and ∂_o denotes the derivative operator in the horizontal/vertical direction. According to the literature review, the above heavy-tailed priors are shown effective for a range of image/video restoration problems. For instance, as α is set as 1, $p(u)$ degenerates to the famous total variation (TV) model which has been exploited for non-blind image/video deblurring in [57, 58], blind image deblurring in [59, 60] and non-blind single-/multi-frame super-resolution in [41, 61]. Nevertheless, it has been empirically proved in [62, 63] that $p(u)$ with α less than 1 usually leads to higher-quality non-blind deblurring and super-resolution results. Specifically, $0.5 \le \alpha \le 0.8$ has been advocated for modeling the heavy-tailed distribution of gradients in the natural scenes.

However, as it turns to blind image restoration, a common consensus has been reached that unnatural image models are required and requested for the success of blur kernel estimation [53], which indicates that ultra-sparse priors should be harnessed to model the distribution of natural image gradients. For example, two unnatural image priors based on the L_α-norm have been exploited for blind image deblurring in [64, 65], wherein the parameter α is set as 0.3 in [64] and a non-increasing sequence 0.8, 0.8, 0.6, 0.6, 0.6, 0.4,…, 0.4 during iteration in [65]. More recently, $p(u)$ defined above is boosted into a family of iteration-specific priors in [66] for blind image deblurring, where each iteration has its own model parameters $\{\gamma(t), \alpha(t)\}$ learned from a training set by a discriminative learning model. However, it should be noted that a counter-intuitive phenomenon has been observed, i.e., the parameter α is allowed to be negative and is found to contribute even more in estimating the coarse shape of blur kernels.

2.2 Spatially Adaptive Heavy-Tailed Priors

Considering both the modeling effectiveness and computational efficiency, a type of new heavy-tailed image priors is proposed to regularize the blur kernel estimation process, expressed as

$$p(u) \propto \prod_{p\in\Omega} \exp\left\{-\gamma_{x,p}(u)\cdot\left|\partial_x u_p\right|^\alpha - \gamma_{y,p}(u)\cdot\left|\partial_y u_p\right|^\alpha\right\}, \tag{1}$$

where $\gamma_{x,p}(u)$ and $\gamma_{y,p}(u)$ are the spatially adaptive weights defined for each image pixel in the horizontal and vertical directions, embodying the core modeling ideas in this paper. On the one hand, $p(u)$ as in (1) is expected potentially discriminative so as to ensure the success of blur kernel estimation, i.e., sharp high-res images should be favored rather than their blurred counterparts and then the delta kernel can be avoided. On the other hand, $p(u)$ as in (1) is expected ease of fast iterative estimation of the nonparametric blur kernel and intermediate sharp image. With a literature review, the first gradient-based influential idea toward discriminative modeling for blind image deblurring is the proposal of normalized sparsity measure [67], whose practical performance is however much questionable according to the results on both synthetic and real-world experiments as indicated in [53, 54]. Another hint from the common consensus that unnatural image priors are desired for kernel estimation is that faint textures/details are harmful to accurate kernel estimation and therefore should be removed in the intermediate sharp image [68–71]. Thus, in order to boost the discriminativeness of the normalized sparsity measure and more importantly its practical performance in kernel estimation, the spatially adaptive weight $\gamma_o(u_p), o \in \{x, y\}$, is presented as

$$\gamma_o(u_p) = \frac{1-\varpi}{\mathcal{G}_o(u)+\varepsilon} + \frac{\varpi}{\mathcal{L}_o(p)+\varepsilon}, \tag{2}$$

where ϖ is a figure between 0 and 1, ε is a small positive value to avoid division by zero, and $\mathcal{G}_o(u)$ and $\mathcal{L}_o(p)$ are defined, respectively, as

$$\mathcal{G}_o(u) = \sqrt{\sum_{p\in\Omega(u)} \left|\partial_o u_p\right|^2} = \|\partial_o u\|_2, \tag{3}$$

$$\mathcal{L}_o(p) = \left|\sum_{q\in\mathcal{N}(p)} \phi_{p,q}\cdot\partial_o u_q\right|, \tag{4}$$

where $\Omega(u)$ denotes the entire image field, $\mathcal{N}(p)$ is a rectangular region centered at the pixel p, and $\phi_{p,q}$ is defined according to the spatial affinity as a distance function of Gaussianity, i.e.,

$$\phi_{p,q} \propto \exp\left(-\frac{(x_p-x_q)^2+(y_p-y_q)^2}{2\sigma^2}\right), \tag{5}$$

where σ is a spatial scale to be specified in implementation.

Now let us dive into (1) and (2) for more details on the modeling behaviors of the proposed heavy-tailed priors. To make it clearer, we study the negative logarithm of $p(u)$ which is denoted as

$$\mathcal{R}(\partial u) \triangleq -\log p(u) = \sum_{p\in\Omega} \gamma_x(u_p)\cdot\left|\partial_x u_p\right|^\alpha + \gamma_y(u_p)\cdot\left|\partial_y u_p\right|^\alpha. \tag{6}$$

That is, $\mathcal{R}(\partial u)$ can be viewed as the deterministic regularization on the image u. We note that the terms $\mathcal{G}_o(u)$ and $\mathcal{L}_o(p)$ were previously used in [67, 72], respectively. Particularly, as α is set to be 1, proposed regularization (6) degenerates to the normalized sparsity measure upon ϖ specified as 0, while to the relative total variation (RTV) upon ϖ specified as 1. Hence, (6) is actually a gradient-based composite model specifically designed for blur kernel estimation. It should be also noted that RTV was originally proposed for structure-preserving image filtering and manipulation, whose value in a window only containing textures is statistically found smaller than that in a window also including structural edges. To the best of our knowledge, none of existing works exploits RTV as a regularization term for nonparametric blind SISR. Hence, it can be intuitively concluded that the core idea of the proposed priors is to amend the generalized normalized sparsity measure $\sum_{p\in\Omega}|\partial_x u_p|^\alpha/\mathcal{G}_x(u)+\sum_p|\partial_y u_p|^\alpha/\mathcal{G}_y(u)$ by the additional generalized RTV $\sum_{p\in\Omega}|\partial_x u_p|^\alpha/\mathcal{L}_x(p)+\sum_p|\partial_y u_p|^\alpha/\mathcal{L}_y(p)$, in the sense that a higher-quality intermediate sharp image with interfering details/textures removed is to be obtained as a critical assurance to accurate kernel estimation. Experimental results along with empirical analysis are to be provided in Sect. 4 for better understanding the inherent superiority of the proposed model.

2.3 Blind Super-Resolution Using Adaptive Heavy-Tailed Priors: A First Look

To formulate the proposed approach to nonparametric blind SR, the low-res imaging process should be firstly clarified.

Let $\mathbf{g}$ be the vector form of the low-res image g with size $N_1 \times N_2$, and $\mathbf{u}$ the vector form of the corresponding high-res image u with size $sN_1 \times sN_2$, where $s > 1$ is an up-sampling factor. Then, the relation between $\mathbf{g}$ and $\mathbf{u}$ can be expressed as two equivalent matrix–vector forms

$$\mathbf{g} = \mathbf{DKu} + \mathbf{n} \tag{7}$$

$$\mathbf{g} = \mathbf{DUk} + \mathbf{n} \tag{8}$$

where $\mathbf{U}$ and $\mathbf{K}$ are assumed as two BCCB (block circulant with circulant blocks) convolution matrices corresponding to the vectorized high-res image $\mathbf{u}$ and blur kernel $\mathbf{k}$, and $\mathbf{D}$ denotes a down-sampling matrix, and $\mathbf{n}$ is the possible zero-mean white Gaussian noise. Note that in implementation image boundaries are smoothed in order to suppress the border artifacts, just the same as in [50]. Then, our task is to infer $\mathbf{u}$ and $\mathbf{k}$ provided only the low-res image $\mathbf{g}$ and the up-sampling factor s. As emphasized above, our proposed adaptive heavy-tailed priors are unnatural since faint details/textures are to be smeared out among the blur kernel estimation. Hence, the nonparametric blind SR task is divided into two independent stages, i.e., (a) alternatingly estimating the nonparametric blur kernel $\mathbf{k}$ and the intermediate high-res image $\mathbf{u}$ using the derived numerical scheme to be specified in Sect. 3; (b) estimating the final sharp high-res image with a state-of-the-art non-blind SR method. As being inspired by [43] and validated in [50], the fundamental TV prior $p(u) \propto \prod_{p\in\Omega}\exp\{-\gamma(|\partial_x u_p| + |\partial_y u_p|)\}$ can serve the non-blind SR problem reasonably in terms of the restoration quality, and therefore, the TV-based fast non-blind SR algorithm specifically proposed in [41] is exploited in this paper. We should note that those more advanced learning-based non-blind SR approaches can be tried, e.g., [11–37], however, which are usually trained with a bicubic kernel. Actually, a more appropriate choice can be tried, i.e., the plug-and-play-based non-blind SR scheme [74], which may incorporate a state-of-the-art image denoiser such as BM3D [76] and the recent CNN-based scheme [97].

As demonstrated in [50], the accuracy of blur kernel estimation for the blind SR task is also affected by the jagging artifacts along the salient edge structures except for the interfering details/textures. Then, the complete formulation for alternatingly estimating the nonparametric blur kernel $\mathbf{k}$ and the intermediate high-res image $\mathbf{u}$ can be given as

$$\hat{\mathbf{u}}, \hat{\mathbf{k}} = \arg\min_{\mathbf{u},\mathbf{k}} \tfrac{\eta}{2}\|\mathbf{g} - \mathbf{DKu}\|_2^2 + \lambda\boldsymbol{\mathcal{R}}(\boldsymbol{\nabla}\mathbf{u}) + \tfrac{\beta}{2}\left\|\breve{\mathbf{u}} - \mathbf{Ku}\right\|_2^2 + \|\mathbf{k}\|_{0.5}^{0.5}, \tag{9}$$

where η, λ, β are positive tuning parameters, $\boldsymbol{\mathcal{R}}(\nabla\mathbf{u})$ is the vectorized form of the regularization term $\mathcal{R}(\partial u)$, and $\boldsymbol{\nabla}\mathbf{u} \triangleq [\boldsymbol{\nabla}_x\mathbf{u};\boldsymbol{\nabla}_y\mathbf{u}]$, wherein $\boldsymbol{\nabla}_x\mathbf{u} = [\partial_x\mathbf{u}_1, \partial_x\mathbf{u}_2, \ldots, \partial_x\mathbf{u}_{sN_1\times sN_2}]^T$, $\boldsymbol{\nabla}_y\mathbf{u} = [\partial_y\mathbf{u}_1, \partial_y\mathbf{u}_2, \ldots, \partial_y\mathbf{u}_{sN_1\times sN_2}]^T$ and $\boldsymbol{\nabla}_x, \boldsymbol{\nabla}_y$ are the convolutional matrices corresponding to the partial derivative operators ∂_x, ∂_y, and the last term is the $L_{0.5}$-norm-based regularization on the blur kernel $\mathbf{k}$ which is an empirical choice just similar to the conventional practice made in the blind deblurring community. To be noted that $\boldsymbol{\mathcal{R}}(\boldsymbol{\nabla}\mathbf{u})$ is responsible for regulating the accurate salient edges as core clues to kernel estimation, which, however, cannot be achieved without the convolutional consistency constraint (CCC) [50], i.e., $\left\|\breve{\mathbf{u}} - \mathbf{Ku}\right\|_2^2$, due to the unavoidable jagging artifacts produced in the naïve up-sampling process. The rationale in the CCC is that using an appropriate learning-based SR model which is generated with a bicubic kernel, the super-resolved blurry image $\breve{\mathbf{u}}$ approximately satisfies the relation $\mathbf{Ku} \approx \breve{\mathbf{u}}$. To gain the idea of proposed energy (9) intuitively, four representative learning-based non-blind SR models are experimented considering their inbred advantages in terms of both accuracy and efficiency, including neighborhood embedding (NE) [12], joint sparse coding (JSC) [16], anchored neighborhood regression (ANR) [24] and deep convolutional network (DCN) [27].

In Fig. 1, the low-res version of a high-res image "bird" is provided, which is blurred by a 19×19 Gaussian kernel

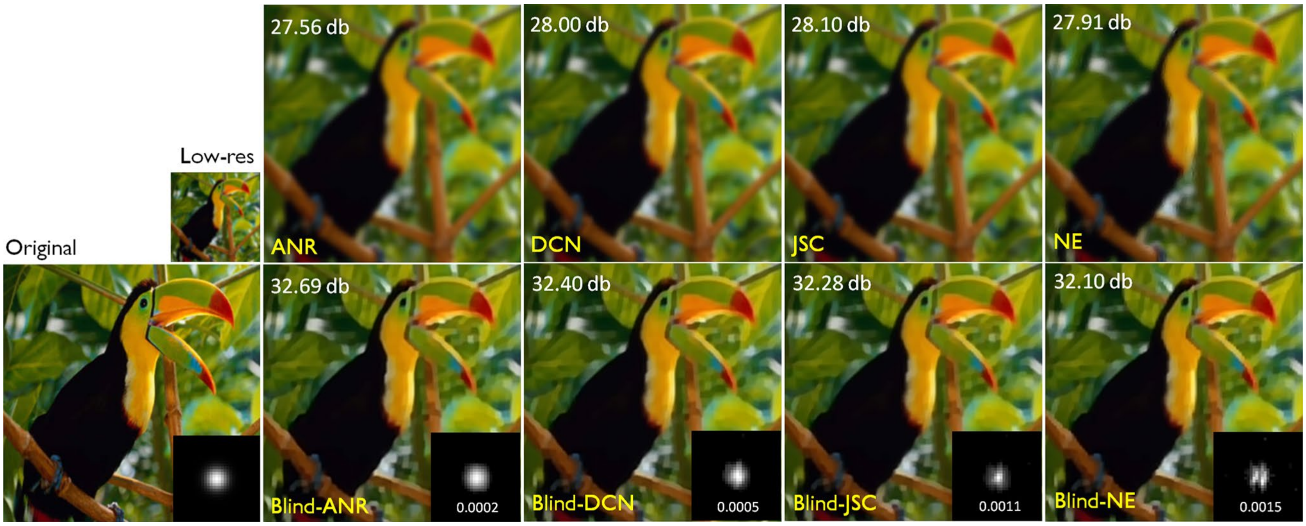

Fig. 1 An illustrative example of the proposed approach to nonparametric blind SR harnessing advanced learning-based methods, including ANR [24], DCN [27], JSC [16], NE [12]. First row: low-res image $\mathbf{g}$ and non-blind super-resolved images $\breve{\mathbf{u}}$; second row: original high-res image $\mathbf{u}$ and blind super-resolved images accompanied by the true and estimated blur kernels. The image PSNR and kernel SSD are calculated and provided for quantitative evaluation. The proposed Blind-ANR has achieved the best performance in terms of image PSNR in this example where the estimated blur kernel most resembles the ground truth in terms of kernel SSD

with *standard deviation* 2.5 and down-sampled by a factor 3. Note that during inference the proposed approach is blind to the blur kernel shape, size and standard deviation. We just assume the kernel size as 31×31 which is normally large enough for the blind SR problem. The true blur kernel is also presented in the first column of Fig. 1 accompanied with the original high-res image "bird." The remaining columns provide the non-blind SR results by the above-mentioned learning-based approaches as well as our blind SR method assisted by each of them, respectively. For example, the second column presents two SR images using ANR [24] and our method assisted by ANR as formulated in (9), simply denoted as Blind-ANR for convenience of description. It is seen that the outputs of four non-blind SR methods [12, 16, 24, 27] are all blurry images, while our blind approach is able to generate visually clear images. The metric PSNR, i.e., peak signal-to-noise ratio, is used to evaluate those non-blind and blind super-resolved images quantitatively. We also use the metric SSD, i.e., sum of squared difference [73], to quantify the error between the estimated blur kernel and its counterpart ground truth. It is apparent that Blind-ANR has achieved the best performance in terms of image PSNR in this example where the estimated blur kernel most resembles the ground truth in terms of kernel SSD. Furthermore, we provide another illustrative example in Fig. 2 where the high-res image "alphabet table" is blurred by a nonparametric motion blur kernel of size 11×11 and down-sampled by a factor 2. We see that Blind-ANR outperforms Blind-DCN, Blind-JSC and Blind-NE by a large margin in terms of image PSNR in this example, and that the four blind approaches also overwhelm the corresponding non-blind counterparts. In the meantime, it is conjectured from this example that the kernel metric SSD may be not absolutely fair for evaluating the performance of nonparametric blind SR approaches. In brief, above two examples demonstrate well the feasibility and effectiveness of our adaptive heavy-tailed image priors and validate that the non-blind SR method ANR [24] can be used as a more robust engine for our framework compared with several other candidates including the advanced deep learning-based method [27]. Not surprisingly, that conforms to the empirical finding in [50]. It is noted that a systematic empirical study can be conducted on the choice of non-blind SR algorithms especially toward those more recent deep learning-based approaches [29–37], which is, however, not the prime focus of this paper.

3 Numerical Algorithm

In order to make the algorithmic description smooth, the vectorized regularization $\mathcal{R}(\boldsymbol{\nabla}\mathbf{u})$ is explicitly written as

$$\mathcal{R}(\nabla\mathbf{u}) \triangleq \boldsymbol{\gamma}_x^T(\mathbf{u})\cdot\mathbf{G}_\alpha(\boldsymbol{\nabla}_x\mathbf{u}) + \boldsymbol{\gamma}_y^T(\mathbf{u})\cdot\mathbf{G}_\alpha(\boldsymbol{\nabla}_y\mathbf{u}), \tag{10}$$

where $\boldsymbol{\gamma}_o^T(\mathbf{u}) \triangleq [\gamma_o(u_{1,1}),\gamma_o(u_{1,2}),\ldots,\gamma_o(u_{1,sN_2});\cdots\ \cdots;\gamma_o(u_{sN_1,1}),\gamma_o(u_{sN_1,2}),\ldots,\gamma_o(u_{sN_1,sN_2})]$ is the vectorized weight, and $\mathbf{G}_\alpha(\boldsymbol{\nabla}_o\mathbf{u}) \triangleq [|\partial_o\mathbf{u}_1|^\alpha,|\partial_o\mathbf{u}_2|^\alpha,\ldots,|\partial_o\mathbf{u}_{sN_1\times sN_2}|^\alpha]^T, o\in\{x,y\}$. We now turn to discuss the numerical scheme for minimizing functional (9) with respect to the intermediate sharp high-res image $\mathbf{u}$ and the nonparametric blur kernel

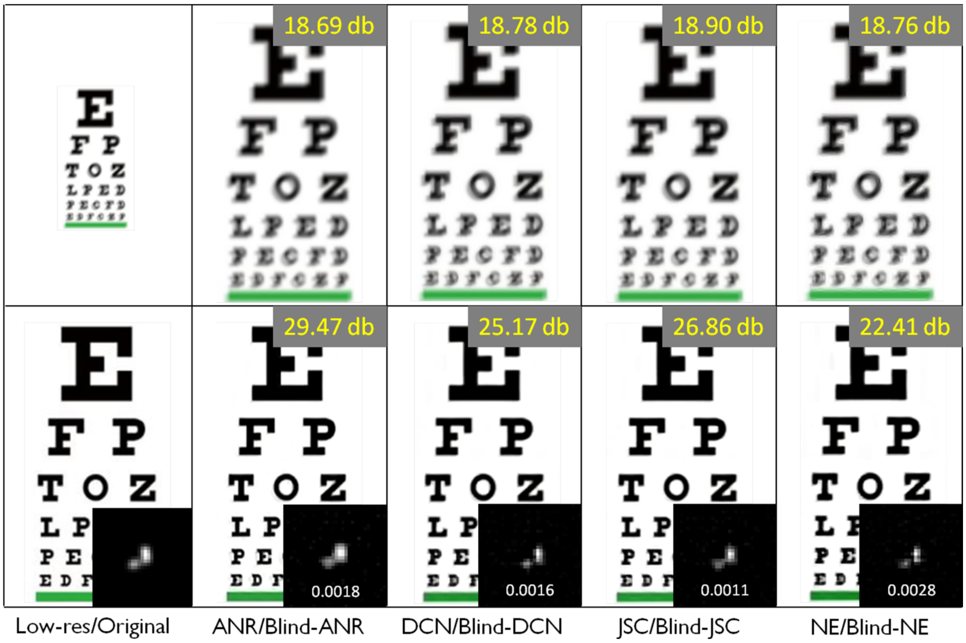

Fig. 2 An illustrative example of the proposed approach to nonparametric blind SR harnessing advanced learning-based methods including ANR [24], DCN [27], JSC [16], NE [12]. First row: low-res image $\mathbf{g}$ and non-blind super-resolved images $\breve{\mathbf{u}}$; second row: original high-res image $\mathbf{u}$ and blind super-resolved images accompanied by the true and estimated blur kernels. The image PSNR and kernel SSD are calculated and provided for quantitative evaluation. The proposed Blind-ANR has achieved the best performance in terms of the PSNR value in this example, however, whose estimated blur kernel does not most resemble the ground truth in terms of the SSD value. Blind super-resolved images can be observed on the computer screen for better visual comparison

$\mathbf{k}$. Here, we do not attempt to provide a rigorous theoretical analysis on the existence of a global minimizer of (9) or further make a claim regarding the convergence of the proposed numerical scheme. Instead, our concentration is on a practical algorithm considering the blind nature of our problem. Normally, the problem can be directly expressed as an alternating minimization of (9), i.e., provided the $(i-1)$ th iterative solutions $\mathbf{u}^{(i-1)}$ and $\mathbf{k}^{(i-1)}$, $\mathbf{u}^{(i)}$ and $\mathbf{k}^{(i)}$ can be obtained by, respectively, solving (11) and (12) as follows

$$\mathbf{u}^{(i)} = \arg\min_{\mathbf{u}} \frac{\eta}{2}\left\|\mathbf{g} - \mathbf{D}\mathbf{K}^{(i-1)}\mathbf{u}\right\|_2^2 + \lambda\mathcal{R}(\mathbf{u}^{(i-1)}, \nabla\mathbf{u}) + \frac{\beta}{2}\left\|\breve{\mathbf{u}} - \mathbf{K}^{(i-1)}\mathbf{u}\right\|_2^2, \tag{11}$$

$$\mathbf{k}^{(i)} = \arg\min_{\mathbf{k}} \frac{\eta}{2}\left\|\mathbf{g} - \mathbf{D}\mathbf{U}^{(i)}\mathbf{k}\right\|_2^2 + \frac{\beta}{2}\left\|\breve{\mathbf{u}} - \mathbf{U}^{(i)}\mathbf{k}\right\|_2^2 + \|\mathbf{k}\|_{0.5}^{0.5}, \tag{12}$$

where $1 \le i \le I = 10$, $\mathbf{K}^{(i-1)}$ and $\mathbf{U}^{(i)}$ are the convolution matrices corresponding to the estimates $\mathbf{k}^{(i-1)}$ and $\mathbf{u}^{(i)}$, and $\mathcal{R}(\mathbf{u}^{(i-1)}, \nabla\mathbf{u})$ is an iterative version of $\mathcal{R}(\nabla\mathbf{u})$ as expressed in (10), i.e.,

$$\mathcal{R}(\mathbf{u}^{(i-1)}, \nabla\mathbf{u}) \triangleq \boldsymbol{\gamma}_x^T(\mathbf{u}^{(i-1)}) \cdot \mathbf{G}_\alpha(\nabla_x\mathbf{u}) + \boldsymbol{\gamma}_y^T(\mathbf{u}^{(i-1)}) \cdot \mathbf{G}_\alpha(\nabla_y\mathbf{u}). \tag{13}$$

3.1 Updating the Intermediate High-Res Image

In this subsection, the well-known ADMM methodology is harnessed to solve non-convex minimization problem (11) by introducing an auxiliary variable $\mathbf{r} \triangleq [\mathbf{r}_x;\mathbf{r}_x]$ which is used to replace $\nabla\mathbf{u} \triangleq [\nabla_x\mathbf{u};\nabla_y\mathbf{u}]$ in (13). We note that although ADMM is known to not always converge in non-convex settings, it can really serve as a powerful heuristic for the blind SR problem considered here.

Specifically, (11) can be now transformed into a constrained problem as

$$\mathbf{u}^{(i)}, \mathbf{r}^{(i)} = \arg\min_{\mathbf{u},\mathbf{r}} \frac{\eta}{2}\left\|\mathbf{g} - \mathbf{D}\mathbf{K}^{(i-1)}\mathbf{u}\right\|_2^2 + \lambda\mathcal{R}(\mathbf{u}^{(i-1)}, \mathbf{r}) + \frac{\beta}{2}\left\|\breve{\mathbf{u}} - \mathbf{K}^{(i-1)}\mathbf{u}\right\|_2^2 \tag{14}$$

$$\text{s.t.} \quad \mathbf{r}_x = \nabla_x\mathbf{u},\ \ \mathbf{r}_y = \nabla_y\mathbf{u}.$$

where $\boldsymbol{\mathcal{R}}(\mathbf{u}^{(i-1)}, \mathbf{r}) \triangleq \boldsymbol{\gamma}_x^T(\mathbf{u}^{(i-1)}) \cdot \mathbf{G}_\alpha(\mathbf{r}_x) + \boldsymbol{\gamma}_y^T(\mathbf{u}^{(i-1)}) \cdot \mathbf{G}_\alpha(\mathbf{r}_y)$. Applying the augmented Lagrangian scheme, we get an unconstrained form of (14) and obtain the iterative estimates of $\mathbf{u}^{(i)}, \mathbf{r}^{(i)}$, i.e.,

$$\begin{aligned}\mathbf{u}_l^{(i-1)}, \mathbf{r}_l^{(i-1)} = \arg\min_{\mathbf{u},\mathbf{r}} \ &\tfrac{\eta}{2}\left\|\mathbf{g} - \mathbf{D}\mathbf{K}^{(i-1)}\mathbf{u}\right\|_2^2 + \lambda\boldsymbol{\mathcal{R}}(\mathbf{u}^{(i-1)}, \mathbf{r}) + \tfrac{\beta}{2}\left\|\breve{\mathbf{u}} - \mathbf{K}^{(i-1)}\mathbf{u}\right\|_2^2 \\ &+ \boldsymbol{\mu}_x^{l-1} \cdot (\boldsymbol{\nabla}_x\mathbf{u} - \mathbf{r}_x) + \tfrac{\zeta_x}{2}\left\|\boldsymbol{\nabla}_x\mathbf{u} - \mathbf{r}_x\right\|_2^2 + \boldsymbol{\mu}_y^{l-1} \cdot (\boldsymbol{\nabla}_y\mathbf{u} - \mathbf{r}_y) + \tfrac{\zeta_y}{2}\left\|\boldsymbol{\nabla}_y\mathbf{u} - \mathbf{r}_y\right\|_2^2,\end{aligned} \tag{15}$$

where $1 \le l \le L = 10, \zeta_x = \zeta_y = \zeta$ is the augmented Lagrangian penalty parameter set as 100 in implementation, and $\mathbf{r}_0^{(i-1)} = \mathbf{0}$, $\mathbf{u}_0^{(i-1)} = \mathbf{u}^{(i-1)}$, $\mathbf{r}_L^{(i-1)} = \mathbf{r}^{(i)}$, $\mathbf{u}_L^{(i-1)} = \mathbf{u}^{(i)}$. As for the Lagrange multipliers $\boldsymbol{\mu}_x^l$, $\boldsymbol{\mu}_y^l$, they are initialized as $\mathbf{0}$ and updated according to the rules

$$\begin{aligned}\boldsymbol{\mu}_x^l &= \boldsymbol{\mu}_x^{l-1} + \zeta\left(\boldsymbol{\nabla}_x\mathbf{u}_l^{(i-1)} - (\mathbf{r}_x)_l^{(i-1)}\right), \\ \boldsymbol{\mu}_y^l &= \boldsymbol{\mu}_y^{l-1} + \zeta\left(\boldsymbol{\nabla}_y\mathbf{u}_l^{(i-1)} - (\mathbf{r}_y)_l^{(i-1)}\right).\end{aligned} \tag{16}$$

Minimizing (15) with respect to $\mathbf{u}$, the intermediate high-res image $\mathbf{u}_l^{(i-1)}$ can be computed as the solution to the following equation

$$\begin{aligned}&\left(\eta(\mathbf{D}\mathbf{K}^{(i-1)})^T\mathbf{D}\mathbf{K}^{(i-1)} + \beta(\mathbf{K}^{(i-1)})^T\mathbf{K}^{(i-1)} + \zeta\left(\boldsymbol{\nabla}_x^T\boldsymbol{\nabla}_x + \boldsymbol{\nabla}_y^T\boldsymbol{\nabla}_y\right)\right)\mathbf{u} \\ &\quad = \eta(\mathbf{D}\mathbf{K}^{(i-1)})^T\mathbf{g} + \beta(\mathbf{K}^{(i-1)})^T\breve{\mathbf{u}} + \zeta\left[\boldsymbol{\nabla}_x^T\left(\mathbf{r}_x - \tfrac{\boldsymbol{\mu}_x}{\zeta}\right) + \boldsymbol{\nabla}_y^T\left(\mathbf{r}_y - \tfrac{\boldsymbol{\mu}_y}{\zeta}\right)\right],\end{aligned} \tag{17}$$

which is solved using the conjugate gradient (CG) algorithm for running efficiency. In the CG, the error tolerance and the maximum number of iterations are, respectively, set as 1e−5 and 15. In implementation, the fast Fourier transform is also exploited to computations involving $\mathbf{K}^{(i-1)}$, $\boldsymbol{\nabla}_x$, $\boldsymbol{\nabla}_y$ and their transposes for further acceleration.

Given the estimate $\mathbf{u}_l^{(i-1)}$, the auxiliary variable $\mathbf{r}_l^{(i-1)}$ is then updated by minimizing the following functional

$$\tfrac{\zeta}{2}\left\|\nabla_x\mathbf{u}_l^{(i-1)} - \mathbf{r}_x + \tfrac{\boldsymbol{\mu}_x^{l-1}}{\zeta}\right\|_2^2 + \tfrac{\zeta}{2}\left\|\nabla_y\mathbf{u}_l^{(i-1)} - \mathbf{r}_y + \tfrac{\boldsymbol{\mu}_y^{l-1}}{\zeta}\right\|_2^2 + \lambda\boldsymbol{\gamma}_x^T(\mathbf{u}^{(i-1)}) \cdot \mathbf{G}_\alpha(\mathbf{r}_x) + \lambda\boldsymbol{\gamma}_y^T(\mathbf{u}^{(i-1)}) \cdot \mathbf{G}_\alpha(\mathbf{r}_y), \tag{18}$$

which can be efficiently solved in a pixel-by-pixel manner, i.e.,

$$\tfrac{\zeta}{2}\left((r_o)_p - \left(\partial_o u_l^{(i-1)} + \tfrac{\mu_o^{l-1}}{\zeta}\right)_p\right)^2 + \lambda\gamma_o\left(u_p^{(i-1)}\right) \cdot \left|(r_o)_p\right|^\alpha, \tag{19}$$

where $p \in \Omega(u)$, and r_o, $u_l^{(i-1)}$, μ_o^{l-1}, $u^{(i-1)}$ are easily obtained by reshaping the vectors $\mathbf{r}_o$, $\mathbf{u}_l^{(i-1)}$, $\boldsymbol{\mu}_o^{l-1}$, $\mathbf{u}^{(i-1)}$ into matrices. Apparently, it now only needs solving a root-finder problem for a general $0 < \alpha \le 1$, i.e., $\min_v \frac{\theta}{2}(w - v)^2 + (v)^\alpha$. It is lucky that we may borrow the numerical idea in [62] for the minimization problem. As for $\alpha = 1, 1/2, 2/3$, analytical solutions can be used as calculated by Algorithms 2 and 3 in [62]; as for other values of α, the numerical root-finder approach Newton–Raphson can be exploited. In this paper, $\alpha = 1$ is found to be a proper choice to the adaptive heavy-tailed priors for nonparametric blind SR, while $\alpha = 1/2$ is a more appropriate candidate for the special blind deblurring problem. More details are to be provided in the experimental part in Sect. 4.

3.2 Updating the Nonparametric Blur Kernel

Turning to estimating the blur kernel $\mathbf{k}^{(i)}$ given the produced image $\mathbf{u}^{(i)}$, our empirical experimentation suggests that the kernel update step can be better performed as implemented in the image derivative domain. Note that this has been also validated in [50] and several blind image deblurring works such as [51, 69, 71]. Therefore, (12) is modified as

$$\begin{aligned}\mathbf{k}^{(i)} = \arg\min_{\mathbf{k}} \sum_{o\in\{x,y\}} &\left\{\tfrac{\eta}{2}\left\|\mathbf{g}_o - \mathbf{D}\mathbf{U}_o^{(i)}\mathbf{k}\right\|_2^2 + \tfrac{\beta}{2}\left\|\breve{\mathbf{u}}_o - \mathbf{U}_o^{(i)}\mathbf{k}\right\|_2^2\right\} \\ &+ \|\mathbf{k}\|_{0.5}^{0.5},\end{aligned} \tag{20}$$

where $\mathbf{g}_o = \boldsymbol{\nabla}_o\mathbf{g}$, $\breve{\mathbf{u}}_o = \boldsymbol{\nabla}_o\breve{\mathbf{u}}$, $\mathbf{U}_o^{(i)}$ denotes the convolutional matrix corresponding to the image gradient $\mathbf{u}_o^{(i)} = \boldsymbol{\nabla}_o\mathbf{u}^{(i)}$. Besides, $\mathbf{k}^{(i)}$ should be projected onto the constraint set $\mathcal{C} = \{\mathbf{k} \ge 0, \ ||\mathbf{k}||_1 = 1\}$ because a blur kernel is nonnegative and normalized.

Notice that (20) is a non-convex minimization problem due to the $L_{0.5}$-norm-based regularization imposed on the blur kernel $\mathbf{k}$. We still build on the ADMM method and derive an iterative numerical algorithm for solving (20), just similar to the one in Sect. 3.1. Let $\mathbf{z}$ be an auxiliary variable used to replace $\mathbf{k}$ in the regularization term, and we obtain

$$\begin{aligned}\mathbf{k}^{(i)}, \mathbf{z}^{(i)} = \arg\min_{\mathbf{k},\mathbf{z}} \sum_{o\in\{x,y\}} &\left\{\tfrac{\eta}{2}\left\|\mathbf{g}_o - \mathbf{D}\mathbf{U}_o^{(i)}\mathbf{k}\right\|_2^2 + \tfrac{\beta}{2}\left\|\breve{\mathbf{u}}_o - \mathbf{U}_o^{(i)}\mathbf{k}\right\|_2^2\right\} \\ &+ \|\mathbf{z}\|_{0.5}^{0.5}, \quad \text{s.t. } \mathbf{k} = \mathbf{z}.\end{aligned} \tag{21}$$

Then, the augmented Lagrangian scheme to (21) can be given for the iterative estimates of $\mathbf{k}^{(i)}, \mathbf{z}^{(i)}$, i.e.,

$$\begin{aligned}&\mathbf{k}_j^{(i-1)}, \mathbf{z}_j^{(i-1)}\\&\quad = \arg\min_{\mathbf{k},\mathbf{z}} \sum_{o\in\{x,y\}} \left\{ \frac{\eta}{2}\left\|\mathbf{g}_o - \mathbf{D}\mathbf{U}_o^{(i)}\mathbf{k}\right\|_2^2 + \frac{\beta}{2}\left\|\breve{\mathbf{u}}_o - \mathbf{U}_o^{(i)}\mathbf{k}\right\|_2^2 \right\}\\&\quad + \|\mathbf{z}\|_{0.5}^{0.5} + \boldsymbol{\mu}_k^{j-1}\cdot(\mathbf{k}-\mathbf{z}) + \frac{\zeta_k}{2}\|\mathbf{k}-\mathbf{z}\|_2^2,\end{aligned} \tag{22}$$

where $1 \le j \le J = 10$, the augmented Lagrangian penalty parameter ζ_k is set as $1e6$ in implementation, and $\mathbf{z}_0^{(i-1)} = \mathbf{0}$, $\mathbf{k}_0^{(i-1)} = \mathbf{k}^{(i-1)}$, $\mathbf{z}_J^{(i-1)} = \mathbf{z}^{(i)}$, $\mathbf{k}_J^{(i-1)} = \mathbf{k}^{(i)}$. Besides, the Lagrange multiplier $\boldsymbol{\mu}_k^j$ is initialized as $\mathbf{0}$ and updated by the rule

$$\boldsymbol{\mu}_k^j = \boldsymbol{\mu}_k^{j-1} + \zeta_k\left(\mathbf{k}_j^{(i-1)} - \mathbf{z}_j^{(i-1)}\right). \tag{23}$$

Obviously, as for $\mathbf{k}_j^{(i-1)}$ it can be easily calculated by solving the following equation

$$\begin{aligned}&\left(\sum_{o\in\{x,y\}} \left\{\eta(\mathbf{D}\mathbf{U}_o^{(i)})^T\mathbf{D}\mathbf{U}_o^{(i)} + \beta(\mathbf{U}_o^{(i)})^T\mathbf{U}_o^{(i)}\right\} + \zeta_k\mathbf{I}\right)\mathbf{k}\\&\quad = \sum_{o\in\{x,y\}} \left\{\eta(\mathbf{D}\mathbf{U}_o^{(i)})^T\mathbf{g}_o + \beta(\mathbf{U}_o^{(i)})^T\breve{\mathbf{u}}_o\right\} + \zeta_k\left(\mathbf{z} - \frac{\boldsymbol{\mu}_k^{j-1}}{\zeta_k}\right),\end{aligned} \tag{24}$$

where $\mathbf{I}$ is the identity matrix. Because of the down-sampling matrix $\mathbf{D}$ involved in (24), the CG method is also used whose error tolerance and maximum iteration number are set the same as those for (17). Additionally, the fast Fourier transform is harnessed to computations involving $\{\mathbf{U}_o^{(i)}\}$ and their transposes for running efficiency.

However, given the estimate $\mathbf{k}_j^{(i-1)}$, the auxiliary variable $\mathbf{z}_j^{(i-1)}$ can be easily updated by minimizing the functional

$$\frac{\zeta_k}{2}\left\|\mathbf{k}_j^{(i-1)} - \mathbf{z} + \frac{\boldsymbol{\mu}_k^{j-1}}{\zeta_k}\right\|_2^2 + \|\mathbf{z}\|_{0.5}^{0.5}, \tag{25}$$

because it has an analytical solution as being demonstrated in [62], just similar to (18).

3.3 Multi-scale Implementation

Following the regular practice in blind image deblurring, a multi-scale strategy is exploited for the final algorithm so as to make our approach applicable to large-scale blur kernel estimation and also avoid getting stuck into poor local minima when solving (11) and (20). The pseudocode of the final algorithm is summarized as Algorithm 1. In each scale, the low-res image $\mathbf{g}$ and the super-resolved blurry image $\breve{\mathbf{u}}$ generated by ANR are 2 times down-sampled successively as inputs to (11) and (20). In the finest scale the inputs are the original $\mathbf{g}$ and $\breve{\mathbf{u}}$ themselves. The initialized image for each scale is set as the down-sampled $\breve{\mathbf{u}}$, and the initialized kernel is set as the bicubic up-sampled blur kernel estimated in the coarser scale (in the coarsest scale the initial kernel is simply set as the Dirac pulse). Furthermore, inspired by the blind deblurring literature the continuation scheme is applied on the parameters η, β for better performance.

It is obvious that the main computational cost of the proposed approach is on the iterative estimates of $\mathbf{u}_l^{(i-1)}$, $\mathbf{k}_j^{(i-1)}$, which are based on the CG algorithm due to the involved down-sampling operator in the low-res imaging model. As proposed adaptive heavy-tailed priors (1) are applied to the degenerated blind deblurring problem to be validated in Sect. 4, $\mathbf{u}_l^{(i-1)}$, $\mathbf{k}_j^{(i-1)}$ can be completely solved via the fast Fourier transform and the finally derived algorithm is to be more efficient. It should be noted that several recent works such as [74, 75] are specifically proposed for fast non-blind super-resolution, which aim to explicitly deal with the down-sampling matrix $\mathbf{D}$ and may be studied for our blind purpose in the future.

Algorithm 1. Blur kernel estimation for nonparametric blind SR

```
input: low-res image $\mathbf{g}$, up-sampling factor $r$, super-resolved image $\breve{\mathbf{u}}$, $\eta$, $\lambda$, $\beta$, $\varpi$.
multi-scale processing: $\{\mathbf{g}_s\}$, $\{\breve{\mathbf{u}}_s\}$, $s \leq 4$.
initializer: $i \leftarrow 0$, $\mathbf{k}^{(0)} \leftarrow$ Dirac pulse, $\mathbf{u}^{(0)} \leftarrow \breve{\mathbf{u}}_1$.
while $s \leq 4$ do
    while $i \leq 10$ do
        • set $\mathbf{u}_0^{(i-1)} \leftarrow \mathbf{u}^{(i-1)}, \mathbf{r}_0^{(i-1)} \leftarrow \mathbf{0}$.
        • solve (11) for $\mathbf{u}^{(i)}$ with 10 iterations of iterative estimates of $\mathbf{u}_l^{(i-1)}, \mathbf{r}_l^{(i-1)}$.
        • set $\mathbf{k}_0^{(i-1)} \leftarrow \mathbf{k}^{(i-1)}, \mathbf{z}_0^{(i-1)} \leftarrow \mathbf{0}$.
        • solve (20) for $\mathbf{k}^{(i)}$ with 10 iterations of iterative estimates of $\mathbf{k}_j^{(i-1)}, \mathbf{z}_j^{(i-1)}$.
        • set $\eta \leftarrow 1.25 \cdot \eta$, $\beta \leftarrow 1.25 \cdot \beta$.
    end while
    • set $i \leftarrow 0$.
    • set $\mathbf{k}^{(0)} \leftarrow$ bicubic up-sampled kernel of scale $s$ with projection onto the set $\mathcal{C}$.
    • set $s \leftarrow s+1$.
    • set $\mathbf{u}^{(0)} \leftarrow \breve{\mathbf{u}}_s$.
end while
output: blur kernel $\hat{\mathbf{k}}$.
non-blind SR: super-resolve the final high-res image using the TV-based SR method [41] given the estimated kernel $\hat{\mathbf{k}}$.
```

4 Experimental Results and Analysis

4.1 Super-Resolving Synthetic Blurred Low-Res Images

This subsection validates the benefit of our method using synthetic blurred low-res images, along with comparisons against two recent state-of-the-art nonparametric blind SR approaches reported in [48, 50]. To be noted that the estimated blur kernels corresponding to [48] were prepared by Dr. Tomer Michaeli who is the first author of [48]. The same TV-based non-blind SR method [41] is used for restoring the final high-res image. Considering the fact that the work in [48] loses its stability for large kernels,[1] we restrict the size of unknown kernels to 19×19 universally across all the experiments in the following. Besides, both the bi-L_0–L_2-norm-based blind SR method [50] and our approach in Algorithm 1 choose ANR [24] for obtaining the non-blind super-resolved image $\breve{\mathbf{u}}$. To quantify the performance of different blur kernel estimation methods, values of PSNR and SSIM corresponding to each of the final super-resolved images are computed. All the experiments are performed using MATLAB v7.0 on a laptop computer with an Intel i7-6700HQ CPU (2.60 GHz) and 12 GB. As for the parameter settings of the proposed method, η, λ, β are specified to be 0.01, 0.25 and 100, respectively. Another parameter to be specified is the balance coefficient ϖ in proposed heavy-tailed image priors (1), which is found to matter a lot to the estimation accuracy and in this paper is fixed as 0.1. For the sake of description clarity, in the following the work in [48] is named Patch Recurrency and that in [50] is named bi-L_0–L_2-norm.

In the first group of synthetic experiments, each of the thirty test images from the Berkeley Segmentation Dataset as shown in Fig. 3 is blurred by a 11×11 Gaussian kernel with *standard deviation* 2.5, down-sampled with a factor 3 and degraded by a zero-mean white Gaussian noise with noise level 1. The blur kernel SSD, image PSNR and image SSIM corresponding to each of compared methods are provided in Table 1. We see that in this scenario the proposed approach has achieved comparable performance to [50] in

---

[1] In [48] blur kernels are typically solved with size 9×9, 11×11 or 13×13 for various blind SR problems.

Fig. 3 Thirty test images from the Berkeley Segmentation Dataset for nonparametric blind SR in the scenario of Gaussian blur

terms of either kernel SSD or image SSIM and PSNR. It is also noticed that the Patch Recurrency method by Michaeli and Irani [48] cannot generate state-of-the-art results in spite of their fresh ideas. For visual perception, the super-resolved images are provided in Figs. 4, 5 and 6 corresponding to images with Nos. 10, 13 and 15, respectively, where the intermediate images produced by the proposed method are also shown. Clearly, it is observed that the estimated blur kernels by [50] and the proposed method are more accurate than those by [48], which actually fails on the image with No. 15 as shown in Fig. 6.

In the second group of experiments, ten high-res images are used to produce blurred low-res images for validating the performance of the proposed approach. Ten synthetic non-Gaussian blur kernels are generated by sampling with a Gaussian process as detailed in [77], all of which are specified to the same size 11×11. Each high-res image is down-sampled with a factor 2 or 3 after the blurring process. Here we just compare [50] and the proposed approach with the super-resolved images shown in Figs. 7, 8, 9, 10, 11, 12, 13, 14, 15 and 16. The values of image PSNR and SSIM are summarized in Table 2. We note that our proposed approach achieves comparatively better performance particularly in terms of image PSNR. The visual perception from the super-resolved images also demonstrates the superiority of the proposed method to some extent. In fact, the advantage of the new adaptive heavy-tailed priors over the bi-L_0–L_2-norm regularization is indeed more obvious in scenarios of motion blur, which is to be demonstrated in Sect. 4.3.

The last group of experiments is to demonstrate the influence of the balance coefficient ϖ on the performance of proposed adaptive priors (1), which is found to work well as fixed to be 0.1. In Figs. 17 and 18, the super-resolved images are provided corresponding to different settings of ϖ for two motion blurred low-res images which are down-sampled 2 and 3 times, respectively; the results of ANR [24] and bi-L_0–L_2-norm [50] are also shown for comparison. It is observed that in both cases $\varpi = 0.1$ has resulted in higher SSIM and PSNR as well as better visual perception as compared against other three settings, i.e., $\varpi = 0$, $\varpi = 0.6$, $\varpi = 1$. In the meantime, our method achieves comparable performance to bi-L_0–L_2-norm [50] in both blind SR experiments.

4.2 Super-Resolving Realistic Blurred Low-Res Images

To check the practical performance of various blind SR approaches, several experiments are conducted on the real-world low-res images. Note that the inputs to each blind approach are only the low-res image $\mathbf{g}$ and the up-sampling factor r. The blur kernels corresponding to Patch Recurrency [48] and bi-L_0–L_2-norm [50] are prepared by the authors. In order to validate the robustness of the proposed method to

Table 1 Nonparametric blind SR in the scenario of Gaussian blur with kernel SSD, image SSIM and image PSNR provided corresponding to Patch Recurrency [48], bi-L_0–L_2-norm [50] and the proposed approach (Ours)

Image no.	[48]			[50]			Ours		
	SSD	SSIM	PSNR	SSD	SSIM	PSNR	SSD	SSIM	PSNR
1	0.0020	0.9322	33.67	0.0006	0.9521	36.04	0.0004	0.9537	36.20
2	0.0017	0.7644	27.06	0.0003	0.8122	29.17	0.0005	0.8104	29.12
3	0.0020	0.6176	26.24	0.0003	0.6587	27.29	0.0007	0.6550	27.20
4	0.0034	0.8177	31.06	0.0004	0.8558	33.79	0.0003	0.8571	33.78
5	0.0030	0.6276	24.94	0.0001	0.6975	27.60	0.0002	0.6975	27.68
6	0.0062	0.6118	23.86	0.0007	0.6987	26.68	0.0002	0.6975	26.63
7	0.0039	0.6443	24.31	0.0001	0.7023	26.71	0.0004	0.6994	26.63
8	0.0062	0.7259	23.44	0.0001	0.7960	25.45	0.0004	0.7886	25.22
9	0.0097	0.3414	17.73	0.0002	0.5351	21.26	0.0004	0.5283	21.20
10	0.0005	0.7376	28.69	0.0003	0.7408	28.74	0.0002	0.7406	28.74
11	0.0044	0.4911	24.64	0.0002	0.5531	27.20	0.0003	0.5539	27.21
12	0.0061	0.5688	23.09	0.0002	0.6567	26.26	0.0002	0.6570	26.35
13	0.0014	0.7367	29.46	0.0004	0.7605	30.94	0.0002	0.7637	31.11
14	0.0014	0.4227	23.70	0.0001	0.4364	24.29	0.0003	0.4347	24.27
15	0.0027	0.7494	28.09	0.0003	0.7819	29.51	0.0001	0.7840	29.63
16	0.0016	0.8676	27.45	0.0007	0.9060	29.77	0.0002	0.9050	29.70
17	0.0016	0.7686	28.97	0.0003	0.7872	29.80	0.0003	0.7874	29.71
18	0.0033	0.8557	28.44	0.0001	0.9105	34.27	0.0001	0.9102	34.33
19	0.0036	0.5815	24.49	0.0003	0.6542	28.24	0.0002	0.6551	28.23
20	0.0026	0.4351	21.74	0.0001	0.4745	22.62	0.0006	0.4668	22.57
21	0.0048	0.5154	20.67	0.0003	0.5347	21.01	0.0005	0.5336	21.00
22	0.0032	0.7041	24.89	0.0001	0.7266	25.60	0.0003	0.7226	25.49
23	0.0044	0.4608	22.86	0.0001	0.5324	24.99	0.0003	0.5304	24.96
24	0.0014	0.6364	26.67	0.0001	0.6607	27.54	0.0002	0.6588	27.52
25	0.0084	0.6586	26.84	0.0002	0.7300	29.73	0.0003	0.7300	29.70
26	0.0041	0.4487	24.44	0.0001	0.5267	27.39	0.0003	0.5236	27.33
27	0.0015	0.5619	24.95	0.0017	0.5853	24.88	0.0002	0.5848	25.22
28	0.0034	0.5965	27.24	0.0001	0.6560	28.86	0.0002	0.6548	28.85
29	0.0039	0.6164	24.31	0.0001	0.6934	26.13	0.0003	0.6920	26.07
30	0.0036	0.5771	23.73	0.0002	0.6638	25.83	0.0003	0.6610	25.79
Average	0.0035	0.6358	25.59	0.0003	0.6893	27.59	0.0003	0.6879	27.58

the parameter settings, they are specified exactly the same as those in the synthetic experiments in Sect. 4.1. In addition, the size of blur kernels for each method is still set as 19×19. We also suggest that one should observe the super-resolved images provided below on the computer screen for better qualitative comparison among different methods.

In Fig. 19, an old photograph is 2 times super-resolved with the blur kernel estimated by each blind approach. It is clearly observed that there are some ringing artifacts along the upper forehead and left shoulder of the young soldier in the result of Michaeli and Irani [48], while the proposed method and bi-L_0–L_2-norm [50] perform much better without noticeable differences in their super-resolved images. In Fig. 20, another old picture is also 2 times super-resolved with different methods. We see that the non-blind approach ANR [24] produces a very blurry image, reflecting the necessity of single-image blind SR techniques. We also observe that both our proposed method and bi-L_0–L_2-norm [50] generate visually pleasant high-res images and also reasonable blur kernels from which it is conjectured

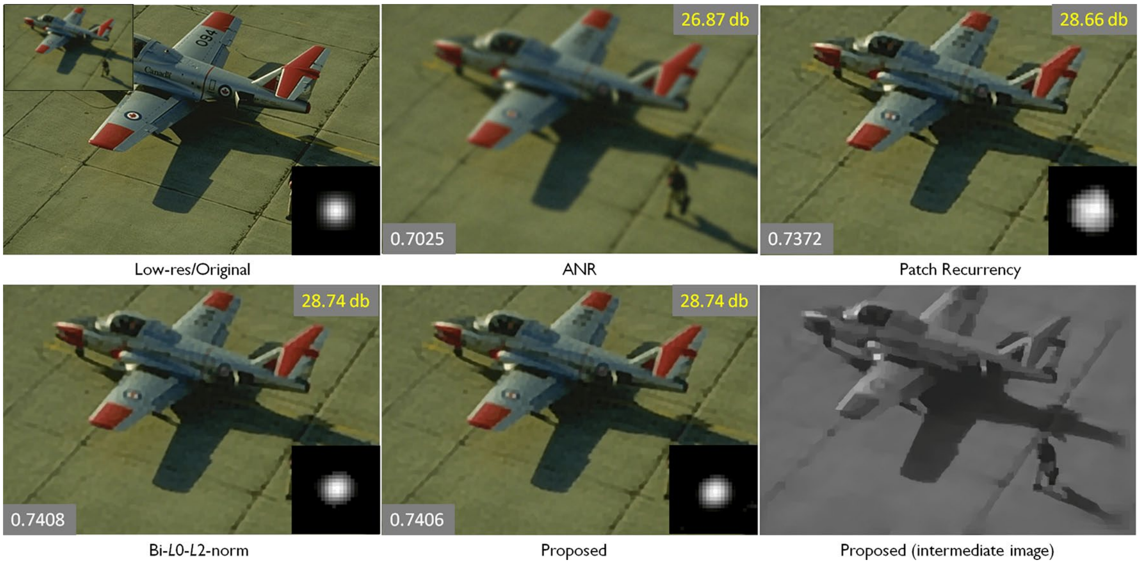

Low-res/Original ANR Patch Recurrency

Bi-*L*0-*L*2-norm Proposed Proposed (intermediate image)

Fig. 4 Super-resolved images along with values of SSIM and PSNR by ANR [24] (0.7025, 26.87 dB), Patch Recurrency [48] (0.7372, 28.66 dB), bi-L_0–L_2-norm [50] (0.7408, 28.74 dB) and our approach (0.7406, 28.74 dB)

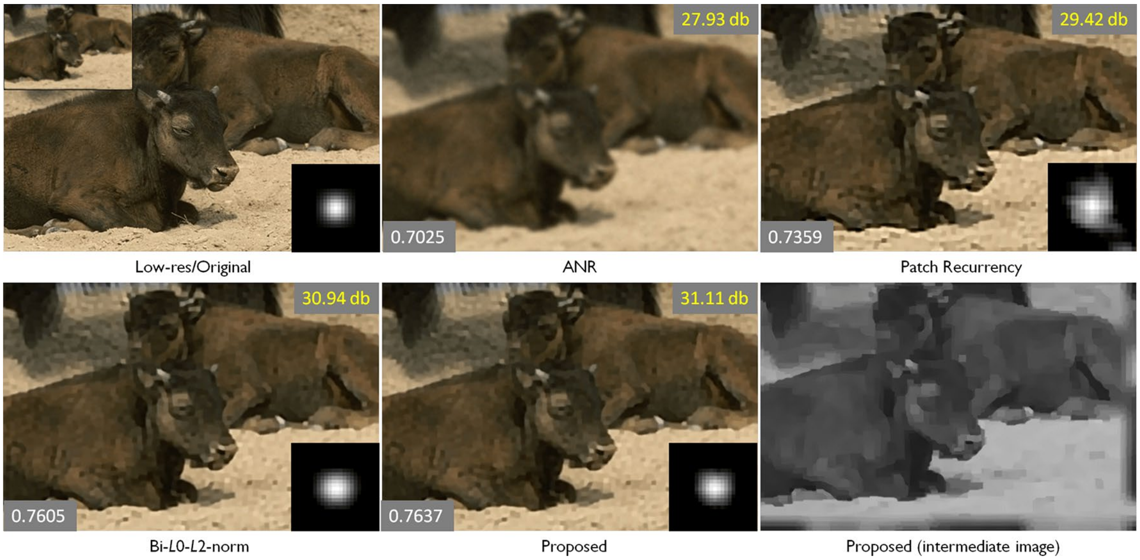

Low-res/Original ANR Patch Recurrency

Bi-*L*0-*L*2-norm Proposed Proposed (intermediate image)

Fig. 5 Super-resolved images along with values of SSIM and PSNR by ANR [24] (0.7025, 27.93 dB), Patch Recurrency [48] (0.7359, 29.42 dB), bi-L_0–L_2-norm [50] (0.7605, 30.94 dB) and our approach (0.7637, 31.11 dB)

that the low-res image had undergone a camera shake blur. In the meanwhile, it is seen that the super-resolved image by the Patch Recurrency approach [48] is very similar to those by the other two algorithms, but a careful inspection tells that the true blur kernel should not have a support as large as that estimated by [48]. In Fig. 21, an iPhone picture is 3 times super-resolved, and the result image by ANR [24] is apparently much blur as compared with the

Fig. 6 Super-resolved images along with values of SSIM and PSNR by ANR [24] (0.7090, 26.68 dB), Patch Recurrency [48] (0.7490, 28.06 dB), bi-L_0–L_2-norm [50] (0.7819, 29.51 dB) and our approach (0.7840, 29.63 dB)

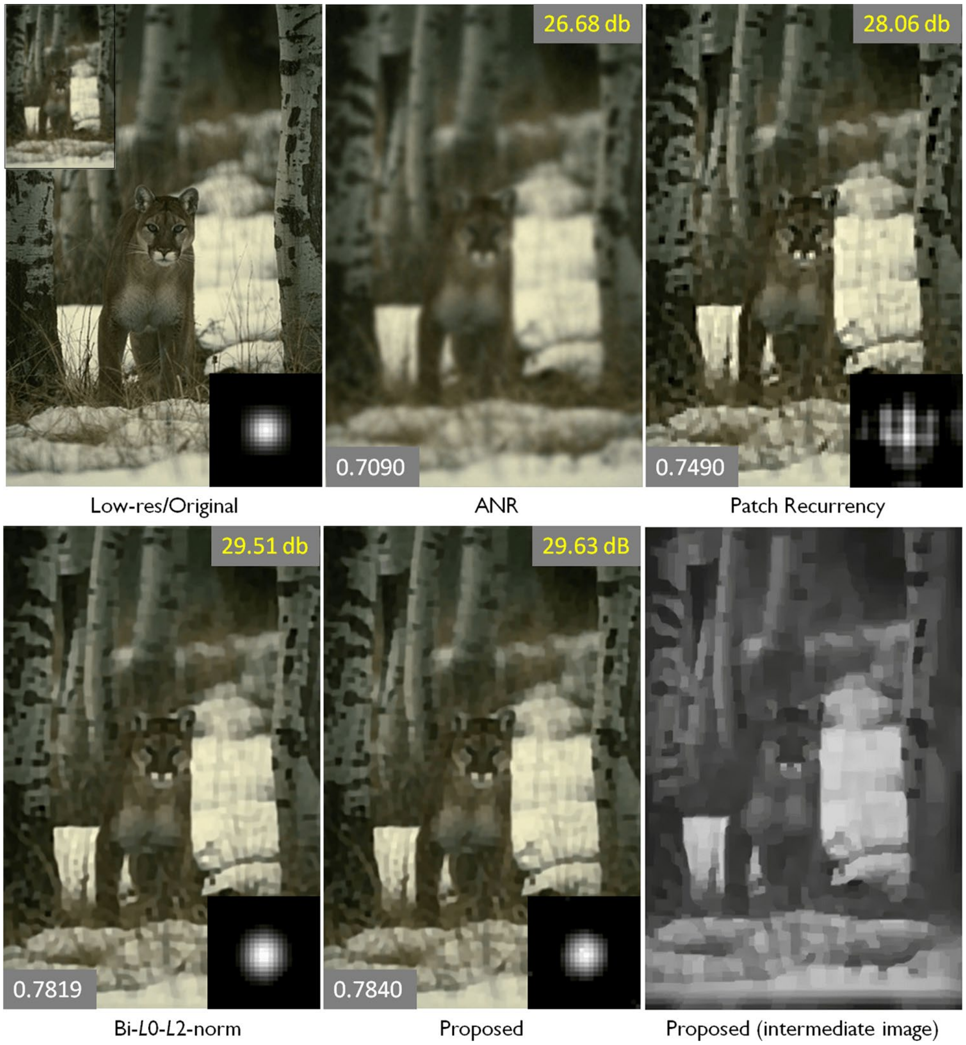

Fig. 7 Super-resolved images (2 times up-sampled) along with values of SSIM and PSNR by ANR [24] (0.8653, 20.17 dB), bi-L_0–L_2-norm [50] (0.9698, 29.24 dB) and our approach (0.9629, 29.63 dB)

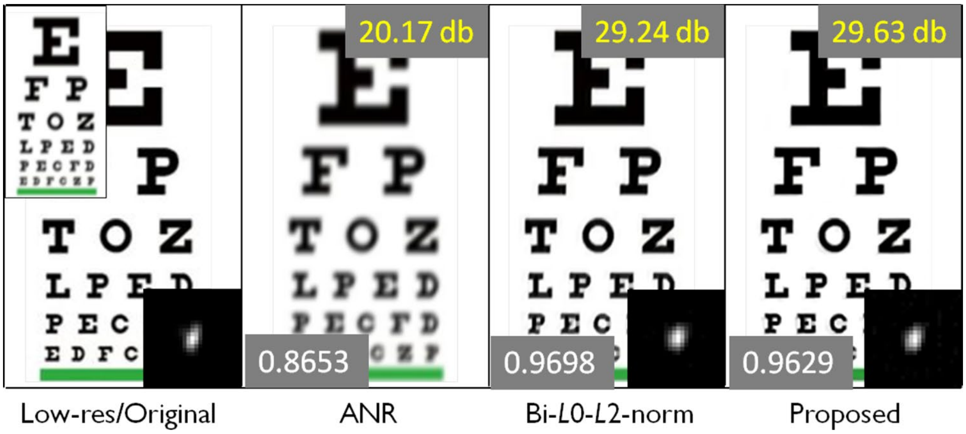

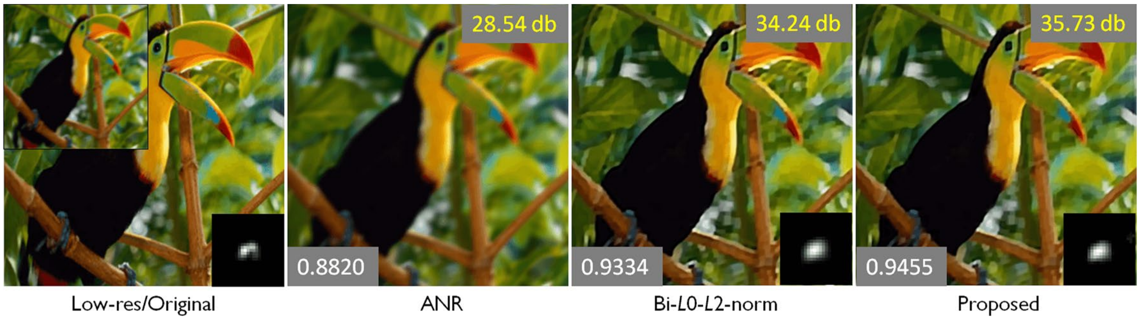

Fig. 8 Super-resolved images (2 times up-sampled) along with values of SSIM and PSNR by ANR [24] (0.8820, 28.54 dB), bi-L_0–L_2-norm [50] (0.9334, 34.24 dB) and our approach (0.9455, 35.73 dB)

Fig. 9 Super-resolved images (2 times up-sampled) along with values of SSIM and PSNR by ANR [24] (0.8820, 28.54 dB), bi-L_0–L_2-norm [50] (0.9334, 34.24 dB) and our approach (0.9455, 35.73 dB)

Fig. 10 Super-resolved images (2 times up-sampled) along with values of SSIM and PSNR by ANR [24] (0.5722, 20.55 dB), bi-L_0–L_2-norm [50] (0.8019, 28.17 dB) and our approach (0.8746, 30.27 dB)

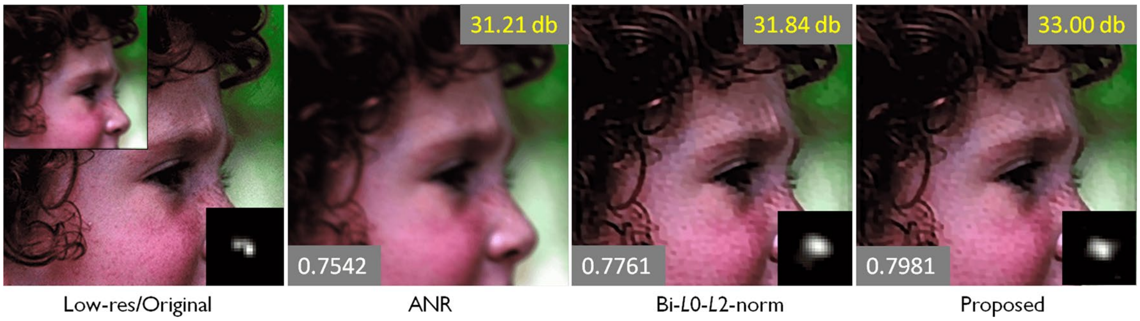

Fig. 11 Super-resolved images (2 times up-sampled) along with values of SSIM and PSNR by ANR [24] (0.7542, 31.21 dB), bi-L_0–L_2-norm [50] (0.7761, 31.84 dB) and our approach (0.7981, 33.00 dB)

Low-res/Original ANR Bi-*L*0-*L*2-norm Proposed

Fig. 12 Super-resolved images (3 times up-sampled) along with values of SSIM and PSNR by ANR [24] (0.7032, 24.28 dB), bi-L_0–L_2-norm [50] (0.7837, 26.14 dB) and our approach (0.7844, 26.20 dB)

Low-res/Original ANR Bi-*L*0-*L*2-norm Proposed

Fig. 13 Super-resolved images (3 times up-sampled) along with values of SSIM and PSNR by ANR [24] (0.4635, 24.48 dB), bi-L_0–L_2-norm [50] (0.6631, 27.34 dB) and our approach (0.6628, 27.45 dB)

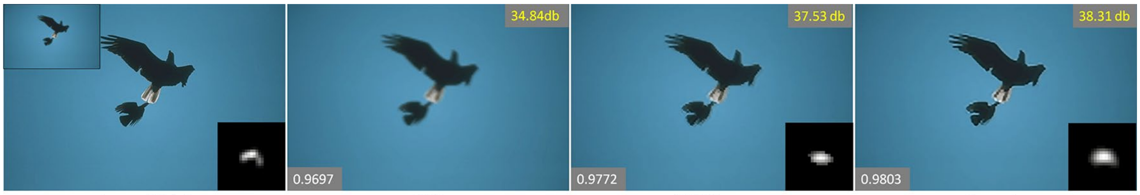

Low-res/Original ANR Bi-*L*0-*L*2-norm Proposed

Fig. 14 Super-resolved images (3 times up-sampled) along with values of SSIM and PSNR by ANR [24] (0.9697, 34.84 dB), bi-L_0–L_2-norm [50] (0.9772, 37.53 dB) and our approach (0.9803, 38.31 dB)

results by the three nonparametric blind methods. Observing the estimated kernels we see that the orientation of the kernel by bi-L_0–L_2-norm [50] resembles a lot that of the kernel by our method, while our kernel support is more accurate because one may inspect that our super-resolved image is visually clearer. Besides, it is noticed the support of the kernel by Patch Recurrency [48] resembles that of the kernel by our approach, but our kernel orientation seems more accurate because of the slightly better visual perception on our super-resolved image. In fact, the superiority of the proposed approach to Patch Recurrency [48] and bi-L_0–L_2-norm [50] is shown more obviously in Fig. 22, where the Patch Recurrency method [48] has completely failed to infer an acceptable blur kernel which leads to a super-resolved image full of ringing and staircase artifacts. As for the bi-L_0–L_2-norm method [50], noticeable ringing artifacts exist in the final super-resolved image due to its inaccurate kernel whose support errors are clearly visible

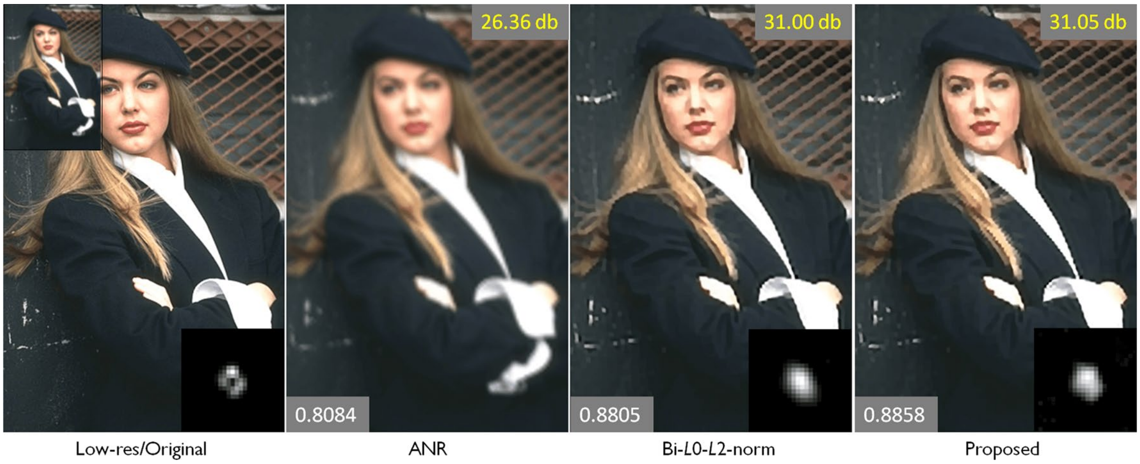

Fig. 15 Super-resolved images (3 times up-sampled) along with values of SSIM and PSNR by ANR [24] (0.8084, 26.36 dB), bi-L_0–L_2-norm [50] (0.8805, 31.00 dB) and our approach (0.8858, 31.05 dB)

Fig. 16 Super-resolved images (3 times up-sampled) along with values of SSIM and PSNR by ANR [24] (0.5059, 24.34 dB), bi-L_0–L_2-norm [50] (0.5666, 25.83 dB) and our approach (0.5665, 25.94 dB)

Table 2 Nonparametric blind SR in the scenario of non-Gaussian blur with image SSIM and PSNR provided corresponding to the compared methods including bi-L_0–L_2-norm [50] and the proposed approach (Ours)

Image no.	[50]		Ours	
	SSIM	PSNR	SSIM	PSNR
1	0.9698	29.24	0.9629	29.63
2	0.9334	34.24	0.9455	35.73
3	0.8949	31.42	0.9226	33.48
4	0.8019	28.17	0.8746	30.27
5	0.7761	31.84	0.7981	33.00
6	0.7837	26.14	0.7844	26.20
7	0.6631	27.34	0.6628	27.45
8	0.9772	37.53	0.9803	38.31
9	0.8805	31.00	0.8858	31.05
10	0.5666	25.83	0.5665	25.94
Average	0.8277	30.28	0.8383	31.11

to the human eyes. Comparatively, the proposed approach achieves the best visual performance in this example. Another low-res image with recurrent patches across scales provided in [48] is also shown in Fig. 23 for comparison. We see that the super-resolved images according to the three blind SR methods are visually almost the same despite that the estimated kernel by our approach is not as accurate as those by Patch Recurrency [48] and bi-L_0–L_2-norm [50]. The last group of experiments is performed on an alphabet table image, and the corresponding super-resolved images are provided in Fig. 24, from which it is observed that the proposed method achieves the best restoration quality. That is because there exist some ringing artifacts in the image corresponding to the Patch Recurrency approach [48] due to the overestimated support of the blur kernel, while the super-resolved image corresponding to bi-L_0–L_2-norm [50] is somewhat blurry due to the underestimated support of the blur kernel.

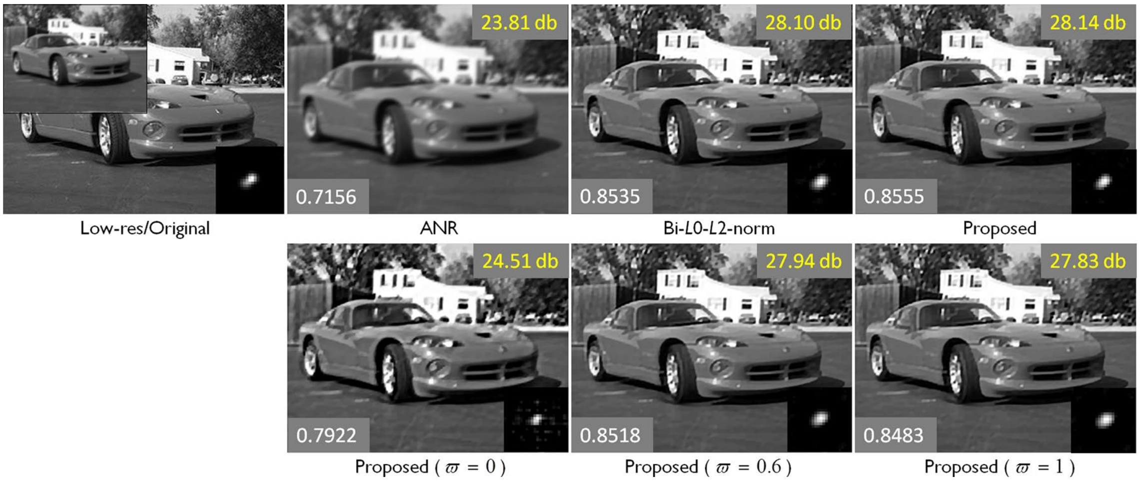

Fig. 17 Super-resolved images (2 times up-sampled) along with values of SSIM and PSNR by ANR [24] (0.7156, 23.81 dB), bi-L_0–L_2-norm [50] (0.8535, 28.10 dB) and our proposed approach (0.8555, 28.14 dB). The second row shows results of the proposed approach provided three other balance coefficients: 0 (0.7922, 24.51 dB), 0.6 (0.8518, 27.94 dB), 1 (0.8483, 27.83 dB)

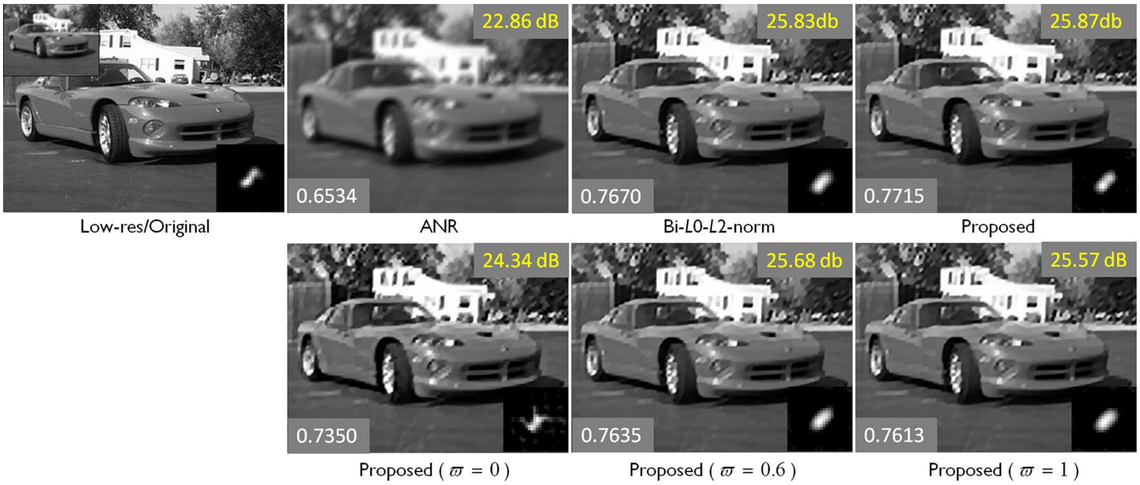

Fig. 18 Super-resolved images (3 times up-sampled) along with values of SSIM and PSNR by ANR [24] (0.7156, 23.81 dB), bi-L_0–L_2-norm [50] (0.8535, 28.10 dB) and our proposed approach (0.8555, 28.14 dB). The second row shows results of the proposed approach provided three other balance coefficients: 0 (0.7922, 24.51 dB), 0.6 (0.8518, 27.94 dB), 1 (0.8483, 27.83 dB)

4.3 Applicability to Blind Image Deblurring

This subsection validates the applicability of the proposed adaptive heavy-tailed priors to nonparametric blind image deblurring. We note that the property of Patch Recurrency across scales in natural images has been also exploited for blind deblurring in [49], and the bi-L_0–L_2-norm regularization was originally proposed in [51] for blind deblurring, too. To make it clear, we formulate the spatially invariant blind deblurring problem into the following functional

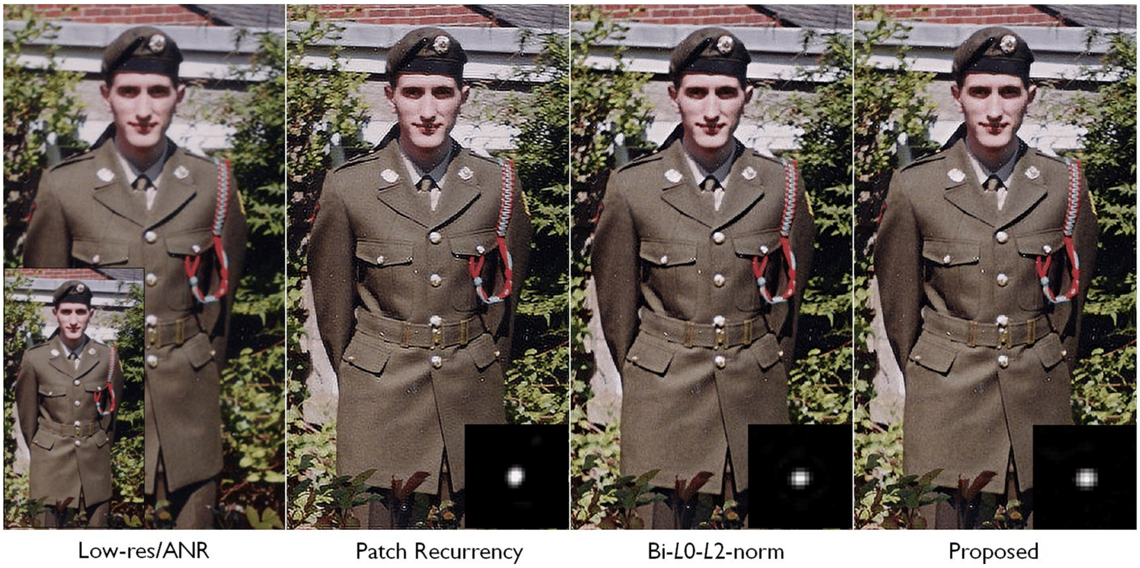

Fig. 19 Blind super-resolution (2 times) by ANR [24], Patch Recurrency [48], bi-L_0–L_2-norm [50] and the proposed approach

Fig. 20 Blind super-resolution (2 times) by ANR [24], Patch Recurrency [48], bi-L_0–L_2-norm [50] and the proposed approach

Fig. 21 Blind super-resolution (3 times) by ANR [24], Patch Recurrency [48], bi-L_0–L_2-norm [50] and the proposed approach

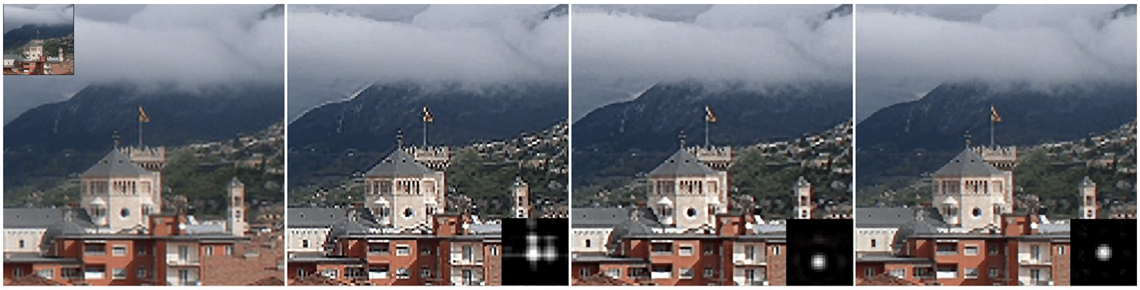

Fig. 22 Blind super-resolution (4 times) by ANR [24], Patch Recurrency [48], bi-L_0–L_2-norm [50] and the proposed approach

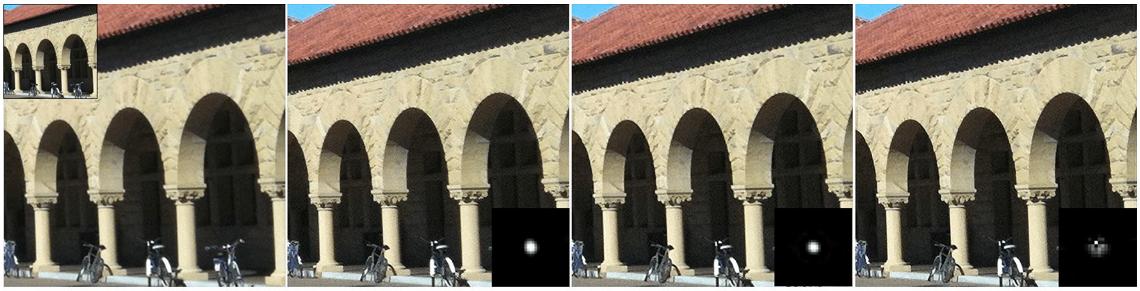

Fig. 23 Blind super-resolution (3 times) by ANR [24], Patch Recurrency [48], bi-L_0–L_2-norm [50] and the proposed approach

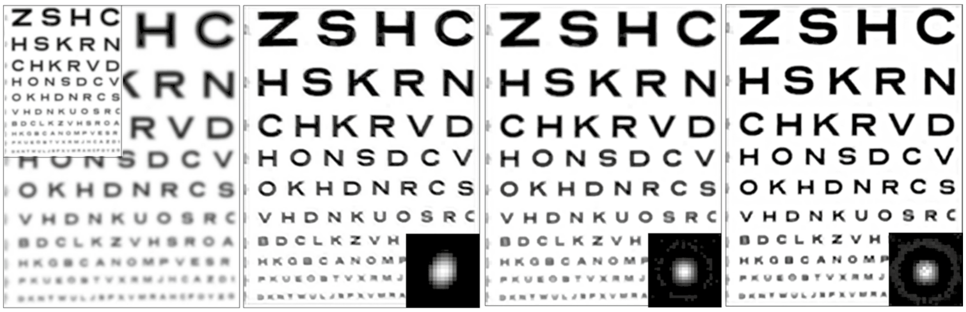

Fig. 24 Blind super-resolution (2 times) by ANR [24], Patch Recurrency [48], bi-L_0–L_2-norm [50] and the proposed approach

$$\hat{\mathbf{u}}, \hat{\mathbf{k}} = \arg\min_{\mathbf{u},\mathbf{k}} \frac{\eta}{2}\|\mathbf{g}-\mathbf{K}\mathbf{u}\|_2^2 + \lambda\mathcal{R}(\nabla\mathbf{u}) + \|\mathbf{k}\|_2^2, \qquad (26)$$

where $\mathcal{R}(\nabla\mathbf{u})$ is the proposed heavy-tailed image priors in (1). Given the blurry image $\mathbf{g}$, the core task is to estimate the blur kernel $\hat{\mathbf{k}}$ with which the final deblurred image can be obtained via the use of an existing non-blind deconvolution method. Here we would like to emphasize the settings of the two parameters in adaptive heavy-tailed priors (1), i.e., the power coefficient α and the balance coefficient ϖ. It is empirically found that ϖ can be fixed as 0.1 which is the same value as the one for Sects. 4.1 and 4.2, while $\alpha = 0.5$ works better in a great many blind deblurring problems.

Fig. 25 Blind deblurring using different models including Patch Recurrency [49], bi-L_0–L_2-norm [51] and our adaptive heavy-tailed priors. The kernel size is set as 99 × 99

In the following, several real-world blind deblurring experiments are performed with comparisons made among the three blind deblurring methods including [49, 51] and Ours. Note that for the sake of fairness, the estimated kernels corresponding to each method are produced under a fixed group of parameter settings; as for non-blind deconvolution, [49] and Ours harness the approach suggested in [56], while [51] exploit the one in [62] which is found to suit [51] better. In each experiment, the intermediate sharp image, estimated blur kernel and final deblurred image are shown for both [51] and our proposed method, while the intermediate image corresponding to [49] cannot be provided since the codes are encapsulated. In Figs. 25 and 26, it is observed that all the three blind approaches have succeeded in estimating the correct motion trajectories, and those of [51] and our approach are slightly more accurate than that of [49] in Fig. 25 because there are some blur and color artifacts in its final deblurred images. Meanwhile, we see that the intermediate images of our approach are somewhat cartoon-like ones, i.e., the fine details/textures in the clear images are removed during the blur kernel estimation, which validate the importance and necessity of the additional generalized RTV in proposed priors (1).

In Fig. 27, it is observed that the proposed method has generated a fairly more accurate blur kernel than the other two methods, whose final deblurred image is apparently of much better visual quality, while there are some blurring and ringing artifacts in that of [49, 51], respectively. Additionally, three text images with multi-scale roof edges are tested in Figs. 28, 29 and 30, observing from which it is found that [49, 51] have completely failed to get a plausible motion trajectory. In spite of that, our approach has achieved impressive performance since its intermediate sharp image, estimated blur kernel and final deblurred image all meet well our expectations.

Fig. 26 Blind deblurring using different models including Patch Recurrency [49], bi-L_0–L_2-norm [51] and our adaptive heavy-tailed priors. The kernel size is set as 35×35

In the following, we would like to show more benefits of the proposed priors for blind deblurring, especially in terms of algorithmic efficiency. Suggested by one of the reviewers, a fair comparison is made among our priors and those in [54, 56]. It should be noted that we totally follow the numerical scheme of [54, 56] and derive a similar algorithm to Algorithm 1 for (26), including the tricks of multi-scale implementation, kernel estimation in the derivative (gradient) domain and continuation strategy applied to the parameter η. Due to the absence of $\mathbf{D}$ in (26) and the simplicity of the L_2-norm regularization on the kernel $\mathbf{k}$, the alternating iterative computations of $\mathbf{u}$ and $\mathbf{k}$ can be made more efficient without the use of the CG as Algorithm 1 for blind super-resolution. Note that the number of outer alternating iterations for updating $\mathbf{u}$ and $\mathbf{k}$ in [54, 56] is set uniformly as 5, which is set the same in our blind deblurring algorithm. As for the inner updating of $\mathbf{u}$, our algorithm obviously requires less iterations than those in [54, 56] since the gradient and intensity components in the priors of [54, 56] have to be minimized in a manner of nested iteration for ensuring accurate blur kernel estimation. For clarity, the core trick of our algorithm is to replace $\nabla\mathbf{u}$ in $\mathcal{R}(\nabla\mathbf{u})$ with another substitute variable like $\mathbf{z}$; thus, minimization over $\mathbf{u}$ is easily simplified and $\mathbf{z}$ can be estimated with a thresholding-style computing scheme as in Algorithm 1.

With the same blurred images in Figs. 25, 26, 27, 28, 29 and 30, we additionally provide another group of experimental results corresponding to the proposed method [54, 56]. The final deblurred images accompanied with their intermediate sharp ones as well as estimated blur kernels as provided in Figs. 31, 32, 33, 34, 35 and 36. The running time of every approach on each deblurred image is given in

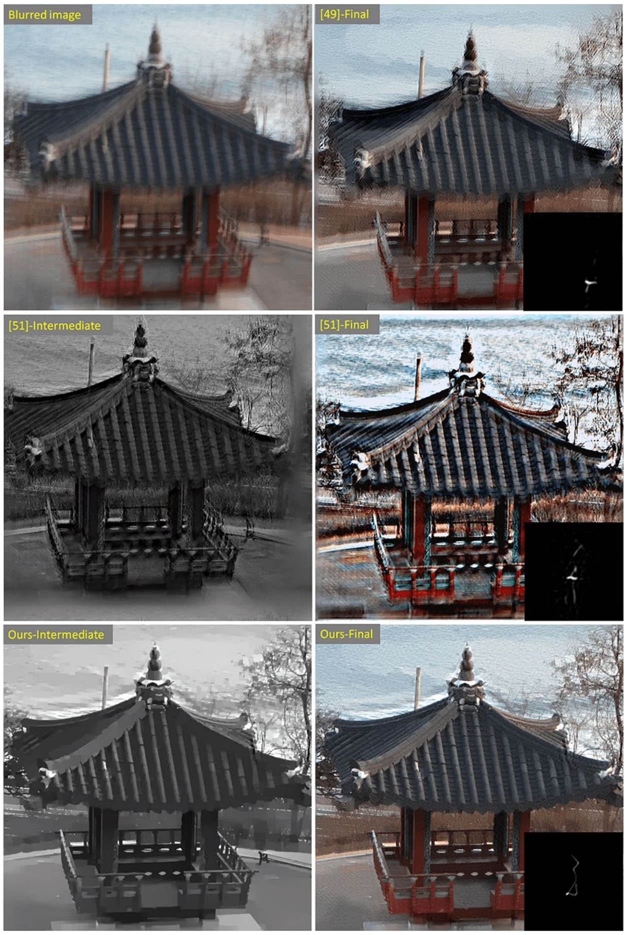

Fig. 27 Blind deblurring using different models including Patch Recurrency [49], bi-L_0–L_2-norm [51] and our adaptive heavy-tailed priors. The kernel size is set as 95 × 95

Table 3. Note that, all the experiments are performed on the same platform as clarified previously.

On the one hand, we observe that most of deblurred images and estimated blur kernels corresponding to the three priors are visually similar to each other. An exception example is the calligraphic work in Fig. 36, where our method apparently produces a more natural deblurred image than [54, 56]. (The differences can be observed clearly on the computer screen.) In spite of that, most of intermediate sharp images corresponding to our priors are slightly different from those corresponding to the priors in [54, 56]. A careful inspection tells that our approach is not only capable of erasing more fine details but also able to avoid false edges, making the intermediate sharp images more appropriate for accurate blur kernel estimation. As a matter of fact, annoying fine textures and details as well as false edges are considered harmful to the accuracy of blur kernel estimation, which has

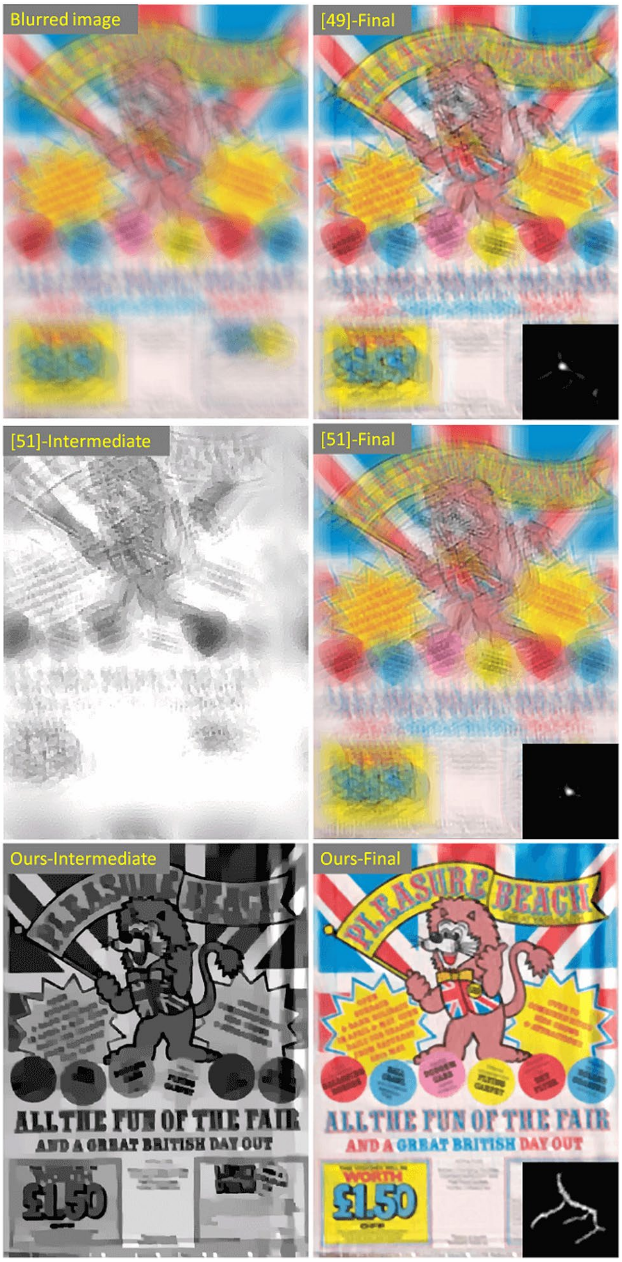

Fig. 28 Blind deblurring using different models including Patch Recurrency [49], bi-L_0–L_2-norm [51] and our adaptive heavy-tailed priors. The kernel size is set as 65 × 65

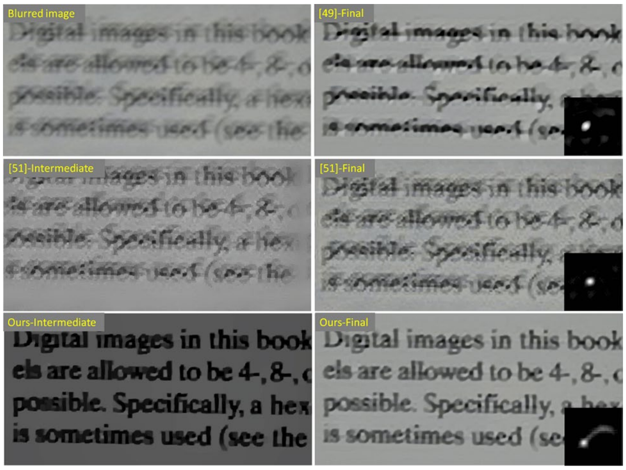

Fig. 29 Blind deblurring using different models including Patch Recurrency [49], bi-L_0–L_2-norm [51] and our adaptive heavy-tailed priors. The kernel size is set as 55×55

been empirically validated in the existing blind deblurring literature, e.g., [69–71]. The calligraphic work in Fig. 36 is such an example. On the other hand, according to Table 3 we find that the proposed method is the most efficient one among the three compared algorithms. Specifically, our method is approximately 2 times faster than [56] and more than 10 times faster than [54]. Note that the comparison on efficiency of different methods here is fair enough and, hence, the proposed image priors are more appropriate for the computationally demanding blind super-resolution problem due to the involvement of the down-sampling matrix $\mathbf{D}$. It is believed that the above explanation verifies what we describe in the introduction part of the paper: *However, nonparametric blind SR with an image prior in either* [56] *or* [54] *will bear a much high computational burden, and hence in terms of the numerical efficiency, neither Pan et al.* [54] *nor Pan et al.* [56] *is a feasible and effective candidate to blind SR*. As for algorithmic schemes along the lines of plug-and-play priors, we indeed derive a plug-and-play-based algorithm with the proposed prior for blind deblurring. Simply speaking, we replace $\mathbf{u}$ instead of $\nabla\mathbf{u}$ in $\mathcal{R}(\nabla\mathbf{u})$ with another substitute variable like $\mathbf{v}$. Thus, minimization over $\mathbf{u}$ is also very efficient. However, it is not the case for $\mathbf{v}$ although its estimation is actually transformed to a filtering/denoising problem with the proposed prior $\mathcal{R}(\mathbf{v})$. We take the blurred image in Fig. 25 for example. Such a plug-and-play-based algorithm runs about 332 s which is much longer

Fig. 30 Blind deblurring using different models including Patch Recurrency [49], bi-L_0–L_2-norm [51] and our adaptive heavy-tailed priors. The kernel size is set as 85×85

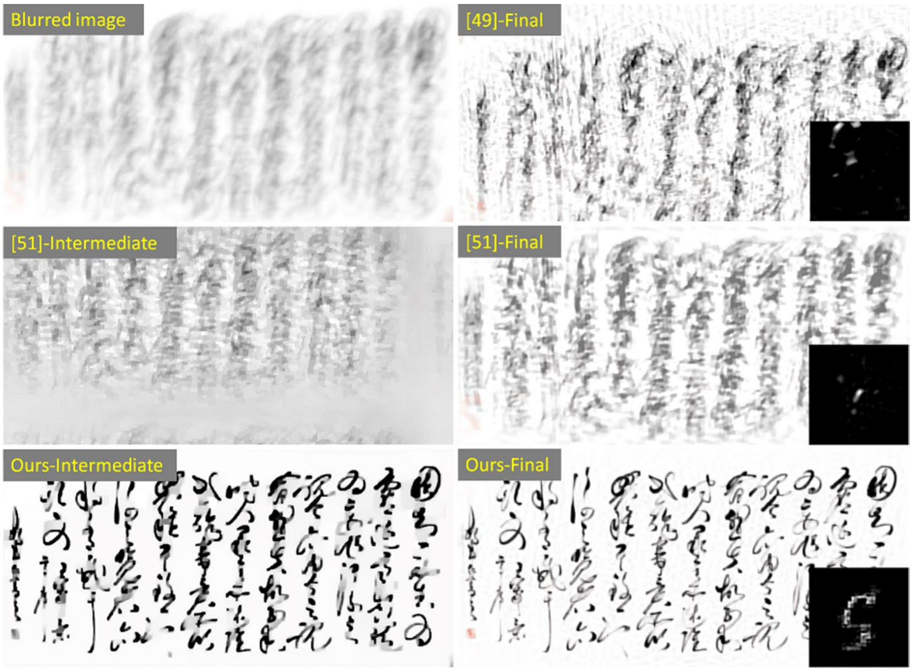

Fig. 31 Comparison of blind deblurring among state-of-the-art image priors in [54, 56] and our adaptive heavy-tailed priors. The kernel size is set as 99×99

than 112 s as shown in Table 3, although visually similar deblurred images are obtained. As for the existing plug-and-play priors with BM3D [76] or recent versions using denoising networks [97], they are not objected specifically to blind deblurring and there are no relevant blind deblurring results reported in the literature, either. Actually, it is common in the literature to use plug-and-play priors for non-blind restoration problems [74].

4.4 Discussions

Though non-blind SISR has achieved fast development by use of CNN-based models as reviewed in Sect. 1, it is not the case for nonparametric blind SR problems. In fact, since the deep architectures for non-blind super-resolution [27–37] and blind image deblurring [77, 90–92] are generally rather different, there are few works addressing nonparametric blind super-resolution for generic natural images. Besides [90–92], two recent works [93, 94] on class-specific blind super-resolution are proposed, which focus on the task of blurred face hallucination. However, they do not apply to generic natural images. For example, in [94] the authors make a comment on their blind method as the following: *When trained on multi-class images, the proposed model is designed to approximate the mixture distribution of the multi-class images. When this mixture distribution becomes too complex, it is difficult to learn a unified model for the diversity of all image classes. Thus, our method is less effective for generic images.*

Indeed, more efforts should be made on deep learning-based nonparametric blind super-resolution of generic

Fig. 32 Comparison of blind deblurring among state-of-the-art image priors in [54, 56] and our adaptive heavy-tailed priors. The kernel size is set as 35 × 35

natural images. However, in the current it is really difficult for us to show at which point the variational approaches for nonparametric blind super-resolution start to dominate the deep learning-based approaches. In fact, we believe the combination of variational and learning-based methods is a more promising direction for both blind super-resolution and blind deblurring.

Lastly, as suggested by one of the reviewers we have performed an additional group of experiments on the realistic blurry low-res image in Fig. 22, where the proposed blind deblurring method in Sect. 4.3 and the dark channel-based blind deblurring method in [54] are first of all utilized to get a deblurred low-res image, and then the state-of-the-art CNN-based super-resolution algorithm [37] is used to generate the final high-res image. We also provide the super-resolution result by direct use of [37] without a step of deblurring. The experimental results are provided in Fig. 37. It is clear that the super-resolved image by Algorithm 1 achieves the best visual quality, while many ringing/distortion artifacts can be observed in the resultant images obtained by a combination of deblurring ([54]/Ours) and CNN-based SR [37]. As we use [37] alone on the blurry low-res image, the super-resolved image is not satisfactory, either, due to the blur artifact just similar to the case of using ANR [24] alone.

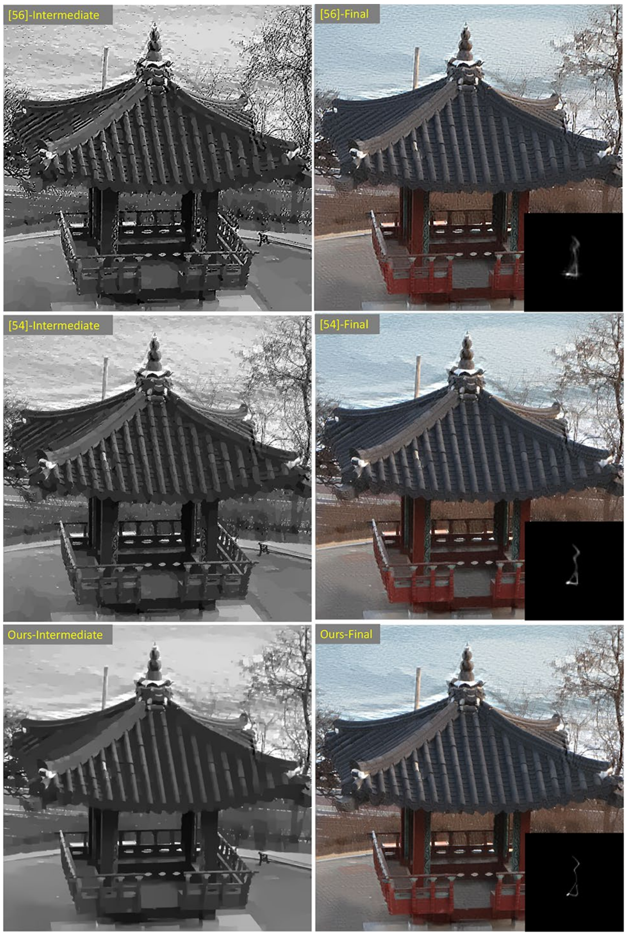

Fig. 33 Comparison of blind deblurring among state-of-the-art image priors in [54, 56] and our adaptive heavy-tailed priors. The kernel size is set as 95 × 95

Fig. 34 Comparison of blind deblurring among state-of-the-art image priors in [54, 56] and our adaptive heavy-tailed priors. The kernel size is set as 65 × 65

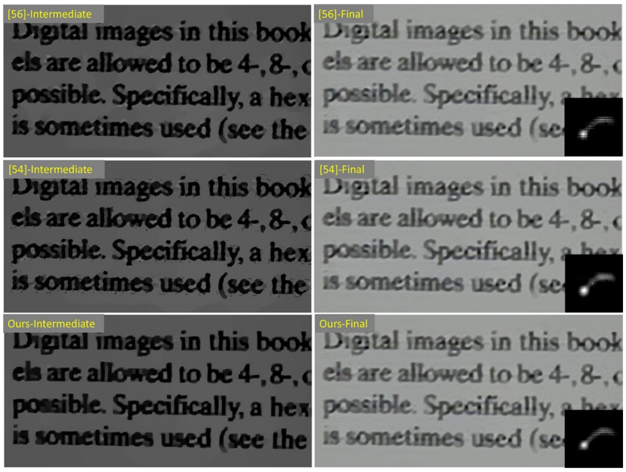

Fig. 35 Comparison of blind deblurring among state-of-the-art image priors in [54, 56] and our adaptive heavy-tailed priors. The kernel size is set as 55 × 55

5 Conclusion

This paper works toward a novel model and fast algorithm for single-image nonparametric blind super-resolution. In specific, a type of adaptive heavy-tailed image priors is introduced incorporating both the model discriminativeness and effectiveness of salient edge pursuit for accurate and reliable blur kernel estimation. With the assistance of proper non-blind SR approaches, e.g., anchored neighborhood regression, nonparametric blind super-resolution can be cast as a new regularized functional minimization problem. An efficient numerical algorithm is derived by harnessing the fast Fourier transform as well as the conjugate gradient method, with which the alternating iterative estimations of kernel and image are lastly implemented in a

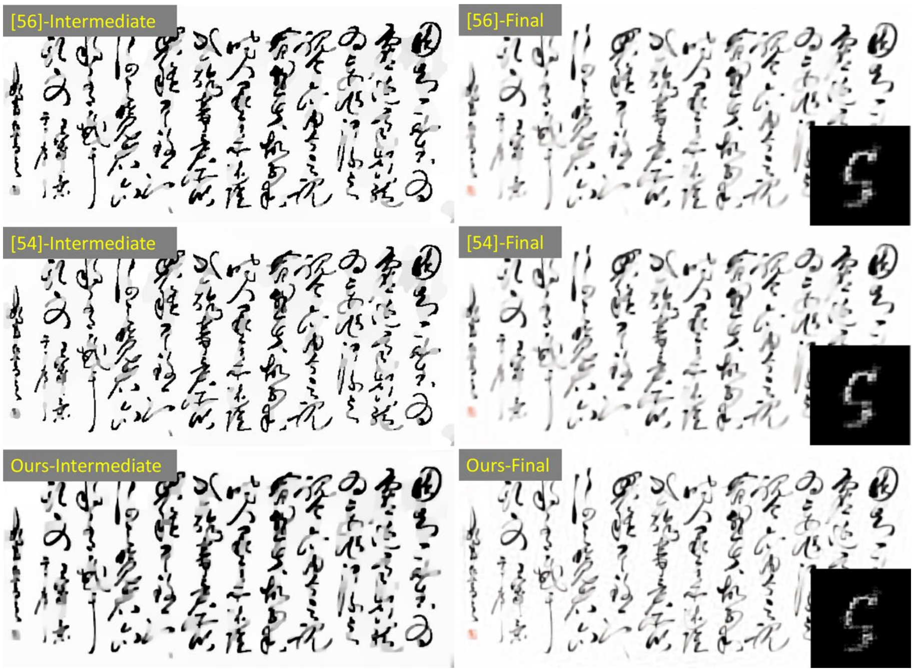

Fig. 36 Comparison of blind deblurring among state-of-the-art image priors in [54, 56] and our adaptive heavy-tailed priors. The kernel size is set as 85×85

Table 3 Running time of blind deblurring with the proposed heavy-tailed image priors and state-of-the-art priors in [54, 56]

Figures	Image resolution	Running time (s)		
		[54]	[56]	Ours
31	455×668	1460	232	112
32	494×701	1058	176	90
33	966×972	3887	688	277
34	572×421	1022	164	78
35	346×702	892	149	74
36	288×596	908	126	63

multi-scale manner. Numerous experiments are performed with the comparisons made among the proposed approach and two recent state-of-the-art ones, i.e., [48, 50], demonstrating that ours is capable of better dealing with low-res images which are probably blurred by various kernels, such as Gaussian-shaped kernels of varying sizes, ellipse-shaped kernels of varying orientations, curvilinear kernels of varying trajectories. As the down-sampling operator is not involved, the proposed algorithmic framework for blind super-resolution is demonstrated quite applicable to the blind image deblurring problem, and experimental results show that the proposed priors achieve more robust deblurring performance than [49, 51] particularly in that the priors not only fit the natural images with multi-scale step edges but also the text images with multi-scale roof edges. Lastly, it is noted that the proposed priors for nonparametric blind super-resolution and deblurring are objected to generic images. We do nothing tailored for the text images either in the design of images priors or in the derivation of numerical scheme. The robust performance of the proposed priors is mainly due to the double principles of discriminativeness as explained in the paper. We should also point out that the non-convexity of gradient penalties cannot ensure the success of blind deconvolution of text images with black and white edges. That is why the L_0-norm-based regularization in both intensity and gradient domains is specifically proposed in [56] for text deblurring and then extended in [54] for generic image deblurring. Comparatively, our method is different from [54, 56] while more efficient than them.

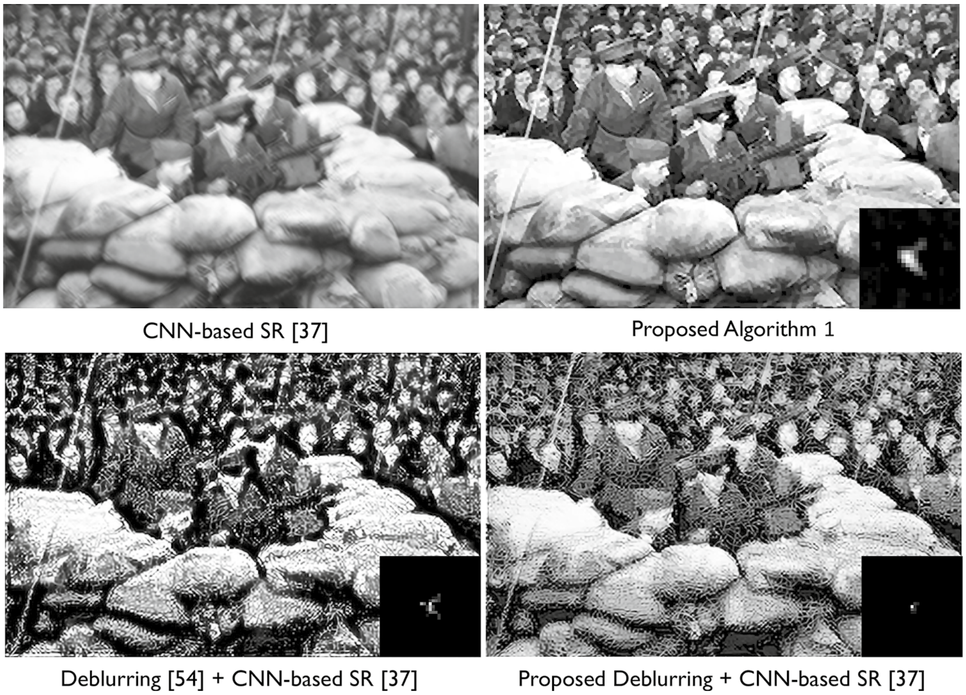

CNN-based SR [37]

Proposed Algorithm 1

Deblurring [54] + CNN-based SR [37]

Proposed Deblurring + CNN-based SR [37]

Fig. 37 Blind super-resolution (2 times) using Algorithm 1 and a combination of blind deblurring ([54]/Ours) and CNN-based SR [37]

Acknowledgements Many thanks are given to the anonymous reviewers for their careful, pertinent and serious comments on this paper which has been strengthened a lot after revision. Wen-Ze Shao is grateful to Prof. Zhi-Hui Wei, Prof. Michael Elad, Prof. Yi-Zhong Ma, Dr. Min Wu and Mr. Ya-Tao Zhang for their kind support in the past years. The study is supported in part by the Natural Science Foundation (NSF) of China (61771250, 61402239, 61602257, 61502244, 11671004), the NSF of Jiangsu Province (BK20160904, BK20150859), the NSF for Jiangsu Institutions (16KJB520035) and the Open Fund of National Engineering Research Center of Communications and Networking (Nanjing University of Posts and Telecommunications, TXKY17008).

References

1. Freeman, W.T., Pasztor, E.C.: Learning to estimate scenes from images. In: Advances in Neural Information Processing Systems (NIPS), pp. 775–781. (1999)
2. Baker S., Kanade, T.: Hallucinating faces. In: Proceedings of IEEE Conference on Automatic Face and Gesture Recognition, pp. 83–88. (2000)
3. Milanfar, P.: Super-Resolution Imaging. CRC Press, Boca Raton (2011)
4. Tian, J., Ma, K.-K.: A survey on super-resolution Imaging. SIViP **5**(3), 329–342 (2011)
5. Nasrollahi, K., Moeslund, T.B.: Super-resolution: a comprehensive survey. Mach. Vis. Appl. **25**, 1423–1468 (2014)
6. Yang, C.-Y., Ma, C., Yang, M.-H.: Single-image super-resolution: a benchmark. In: Proceedings of European Conference on Computer Vision (ECCV), pp. 372–386. (2014)
7. Goodfellow, I., Bengio, Y., Courville, A.: Deep Learning. MIT Press, Cambridge (2016)
8. LeCun, Y., Yoshua, B., Hinton, G.: Deep learning. Nature **521**(7553), 436–444 (2015)
9. Schmidhuber, J.: Deep learning in neural networks: an overview. Neural Networks **61**, 85–117 (2015)
10. Krizhevsky, A., Sutskever, I., Hinton, G.: ImageNet classification with deep convolutional neural networks. Adv Neural Inform Process Syst (NIPS) **25**(2), 1097–1105 (2012)
11. Bevilacqua, M., Roumy, A., Guillemot, C., Morel, M.-L.A.: Low-complexity single-Image super-resolution based on nonnegative neighbor embedding. In: British Machine Vision Conference pp. 1–10. (2012)
12. Chang, H., Yeung, D.-Y., Xiong, Y.: Super-resolution through neighbor embedding. In: IEEE International Conference on Computer Vision and Pattern Recognition (CVPR), pp. 275–282. (2004)
13. Zhang, K., Gao, X., Li, X., Tao, D.: Partially supervised neighbor embedding for example-based image super-resolution. IEEE J. Sel. Top. Signal Process. **5**(2), 230–239 (2011)
14. Gao, X., Zhang, K., Li, X., Tao, D.: Joint learning for single-image super-resolution via a coupled constraint. IEEE Trans. Image Process. **21**(2), 469–480 (2012)
15. Yang, J., Wright, J., Huang, T.S., Ma, Y.: Image super-resolution via sparse representation. IEEE Trans. Image Process. **19**(11), 2861–2873 (2010)
16. Zeyde, R., Elad, M., Protter, M.: On single image scale-up using sparse representation. Int. Conf. Curves Surf. **6920**, 711–730 (2010)
17. Yang, J., Wang, Z., Lin, Z., Cohen, S., Huang, T.: Coupled dictionary training for image super-resolution. IEEE Trans. Image Process. **21**(8), 3467–3478 (2012)
18. Tang, Y., Yuan, Y., Yan, P., Li, X.: Greedy regression in sparse coding space for single-image super-resolution. J. Vis. Commun. Image Represent. **24**(2), 148–159 (2013)
19. Peleg, T., Elad, M.: A statistical prediction model based on sparse representations for single image super-resolution. IEEE Trans. Image Process. **23**(6), 2569–2582 (2014)

20. Purkait, P., Chanda, B.: Image upscaling using multiple dictionaries of natural image patches. In: Lecture Notes in Computer Science (11th Asian Conference on Computer Vision), vol. 7726, pp. 284–295. (2013)
21. He, L., Qi, H., Zaretzki, R.: Beta process joint dictionary learning for coupled feature spaces with application to single image super-resolution. In: IEEE Conference on Computer Vision and Pattern Recognition (CVPR), pp. 345–352. (2013)
22. Wang, S., Zhang, L., Liang, Y., Pan, Q.: Semi-coupled dictionary learning with applications to image super-resolution and photo-sketch synthesis. In: IEEE Conference on Computer Vision and Pattern Recognition (CVPR), pp. 2216–2223. (2012)
23. Jia, K., Tang, X., Wang, X.: Image transformation based on learning dictionaries across image spaces. IEEE Trans. Pattern Anal. Mach. Intell. (PAMI) **35**(2), 367–380 (2013)
24. Timofte, R., De Smet, V., Van Gool, L.: Anchored neighborhood regression for fast example-based super-resolution. In: IEEE International Conference on Computer Vision (ICCV), pp. 1920–1927. (2013)
25. Timofte, R., De Smet, V., Van Gool, L.: A+: Adjusted anchored neighborhood regression for fast super-resolution. In: Asian Conference on Computer Vision (ACCV), pp. 111–126. (2014)
26. Schulter, S., Leistner, C., Bischof, H.: Fast and accurate image upscaling with super-resolution forests. In: IEEE International Conference on Computer Vision and Pattern Recognition. (CVPR), pp. 3791–3799, (2015)
27. Dong, C., Loy, C.C., He, K., Tang, X.: Learning a deep convolutional network for image super-resolution. In: European Conference on Computer Vision (ECCV), pp. 184–199. (2014)
28. Cui, Z., Chang, H., Shan, S., Zhong, B., Chen, X.: Deep network cascade for image super-resolution. In: European Conference on Computer Vision (ECCV), pp. 49–64. (2014)
29. Kim, J., Kwon Lee, J., Mu Lee, K.: Accurate image super-resolution using very deep convolutional networks. In: IEEE Conference Computer Vision and Pattern Recognition (CVPR), pp. 1646–1654. (2015)
30. Kim, J., Kwon Lee, J., Mu Lee, K.: Deeply-recursive convolutional network for image super-resolution. In: IEEE Conference on Computer Vision and Pattern Recognition (CVPR), pp. 1637–1645. (2015)
31. Johnson, J., Alahi, A., Fei-Fei, L.: Perceptual losses for real-time style transfer and super-resolution. In: European Conference on Computer Vision (ECCV), pp. 694–711. (2016)
32. Wang, Z., Liu, D., Yang, J., Han, W., Huang, T.: Deep networks for image super-resolution with sparse prior. In: IEEE Conference on Computer Vision (ICCV), pp. 370–378. (2015)
33. Bruna, J., Sprechmann, P., LeCun, Y.: Super-resolution with deep convolutional sufficient statistics. In: International Conference on Learning Representation (ICLR), (2016)
34. Dong, C., Loy, C.C., Tang, X.: Accelerating the super-resolution convolutional neural network. In: European Conference on Computer Vision (ECCV), pp. 391–407. (2016)
35. Shi, W., Caballero, J., Huszar, F., et al.: Real-time single image and video super-resolution using an efficient sub-pixel convolutional neural network. In: IEEE Conference on Computer Vision and Pattern Recognition (CVPR), pp. 1874–1883. (2016)
36. Sajjadi, M., Scholkopf, B., Hirsch, M.: EnhanceNet: single image super-resolution through automated texture synthesis. arXiv preprint arXiv:1612.07919, (2016)
37. Lim, B., Son, S., Kim, H., Nah, S., Lee, K.M.: Enhanced deep residual networks for single image super-resolution. In: IEEE Conference on Computer Vision and Pattern Recognition Workshops (CVPRW), Honolulu, pp. 1132–1140. (2017)
38. Zhu, S., Liu, S., Loy, C.C., Tang, X.: Deep cascaded bi-network for face hallucination. In: European Conference on Computer Vision (ECCV), pp. 614–630. (2016)
39. Yu, X., Porikli, F.: Ultra-resolving face images by discriminative generative networks. In: European Conference on Computer Vision (ECCV), pp. 318–333. (2016)
40. Fattal, R.: Image upsampling via imposed edge statistics. ACM Trans. Graph. **26**, Article No. 95, (2007)
41. Marquina, A., Osher, S.J.: Image super-resolution by TV-regularization and Bregman iteration. J. Sci. Comput. **37**, 367–382 (2008)
42. Dong, W., Zhang, L., Shi, G., Li, X.: Nonlocally centralized sparse representation for image restoration. IEEE Trans. Image Process. **22**(4), 1620–1630 (2013)
43. Efrat, N., Glasner, D., Apartsin, A., Nadler, B., Levin, A.: Accurate blur models vs. image priors in single image super-resolution. In: IEEE Conference on Computer Vision (ICCV), pp. 2832–2839. (2013)
44. Begin, I., Ferrie, F.R.: PSF recovery from examples for blind super-resolution. IEEE Conference on Image Processing (ICIP), pp. 421–424. (2007)
45. Wang, Q., Tang, X., Shum, H.: Patch based blind image super resolution. In: IEEE Conference on Computer Vision (ICCV), pp. 709–716. (2005)
46. He, Y., Yap, K.H., Chen, L., Chau, L.P.: A soft MAP framework for blind super-resolution image reconstruction. Image Vis. Comput. **27**, 364–373 (2009)
47. Joshi, N., Szeliski, R., Kriegman, D.J.: PSF estimation using sharp edge prediction. In: IEEE Conference on Computer Vision and Pattern Recognition (CVPR), pp. 1–8. (2008)
48. Michaeli, T., Irani, M.: Nonparametric blind super-resolution. In: IEEE Conference on Computer Vision (ICCV), pp. 945–952. (2013)
49. Michaeli, T., Irani, M.: Blind deblurring using internal patch recurrence. In: European Conference on Computer Vision (ECCV), pp. 783–798. (2014)
50. Shao, W., Elad, M.: Simple, accurate, and robust nonparametric blind super-resolution. In: Zhang, Y.J. (ed.) ICIG 2015 Part III Lecture Notes in Computer Science, vol. 9219, pp. 333–348. Springer, Cham (2015)
51. Shao, W., Li, H., Elad, M.: Bi-L_0–L_2-norm regularization for blind motion deblurring. J. Vis. Commun. Image Represent. **33**, 42–59 (2015)
52. Fergus, R., Singh, B., Hertzmann, A., Roweis, S.T., Freeman, W.T.: Removing camera shake from a single photograph. ACM Trans. Graph. **25**(3), 787–794 (2006)
53. Lai, W.S., Huang, J.B., Hu, Z., Ahuja, N., Yang, M.H.: A comparative study for single image blind deblurring. In: IEEE Conference on Computer Vision and Pattern Recognition (CVPR), pp. 1701–1709. (2016)
54. Pan, J., Sun, D., Pfister, H., Yang, M.H.: Blind image deblurring using dark channel prior. In: IEEE Conference on Computer Vision and Pattern Recognition (CVPR), pp. 1628–1636. (2016)
55. Pan, J., Hu, Z., Su, Z., Yang, M.-H.: Debluring low-resolution images. In: Lecture Notes in Computer Science. ACCV 2016 Workshops, Part I, vol. 10116, pp. 111–127. (2017)
56. Pan, J., Hu, Z., Su, Z., Yang, M.-H.: Deblurring text images via L_0-regularized intensity and gradient prior. In: IEEE International Conference on Computer Vision and Pattern Recognition (CVPR), pp. 1628–1636. (2014)
57. Rudin, L., Osher, S.: Total variation based image restoration with free local constraints. In: Proceedings of 1st IEEE International Conference on Image Processing (ICIP), Austin, pp. 31–35. (1994)
58. Chan, S.H., Khoshabeh, R., Gibson, K.B., Gill, P.E., Nguyen, T.Q.: An augmented Lagrangian method for total variation video restoration. IEEE Trans. Image Process. **20**(11), 3097–3111 (2011)
59. Chan, T.F., Wong, C.K.: Total variation blind deconvolution. IEEE Trans. Image Process. **7**(3), 370–375 (1998)

60. Perrone, D., Favaro, P.: A clearer picture of total variation blind deconvolution. IEEE Trans. Pattern Anal. Mach. Intell. **38**(6), 1041–1055 (2016)
61. Ng, M.K., Weiss, P., Yuan, X.: Solving constrained total-variation image restoration and reconstruction problems via alternating direction methods. SIAM J. Sci. Comput. **32**, 2710–2736 (2010)
62. Krishnan, D., Fergus, R.: Fast image deconvolution using hyper-laplacian priors. In: Proceedings of International Conference on Neural Information and Processing Systems (NIPS), pp. 1033–1041. (2009)
63. Tappen, M.F., Russel, B.C., Freeman, W.T.: Exploiting the sparse derivative prior for super-resolution and image demosaicing. In: Proceedings of IEEE Workshop on Statistical and Computational Theories of Vision. (2003)
64. Kotera, J., Sroubek, F., Milanfar, P.: Blind deconvolution using alternating maximum a posteriori estimation with heavy-tailed priors. In: Wilson, R. et al. (eds.) Lecture Notes in Computer Science CAIP, Part II, vol. 8048, pp. 59–66. (2013)
65. Almeida, M., Almeida, L.: Blind and semi-blind deblurring of natural images. IEEE Trans. Image Processing **19**(1), 36–52 (2010)
66. Zuo, W., Ren, D., Gu, S., Lin, L., Zhang, L.: Learning iteration-wise generalized shrinkage–thresholding operators for blind deconvolution. IEEE Trans. Image Process **25**(4), 1751–1764 (2016)
67. Krishnan, D., Tay, T., Fergus, R.: Blind deconvolution using a normalized sparsity measure. IEEE Conference on Computer Vision and Pattern Recognition (CVPR), pp. 233–240. (2011)
68. Money, J.H., Kang, S.H.: Total variation minimizing blind deconvolution with shock filter reference. Image Vis. Comput. **26**(2), 302–314 (2008)
69. Cho, S., Lee, S.: Fast motion deblurring. ACM Trans. Graph. **28**(5), Article No. 145. (2009)
70. Xu, L., Jia, J.: Two-phase kernel estimation for robust motion deblurring. In: European Conference on Computer Vision, Part I, LNCS 6311, pp. 157–170. (2010)
71. Xu, L., Zheng, S., Jia, J.: Unnatural L_0 sparse representation for natural image deblurring. In: IEEE Conference on Computer Vision and Pattern Recognition, pp. 1107–1114. (2013)
72. Xu, L., Yan, Q., Xia, Y., Jia, J.: Structure extraction from texture via relative total variation. ACM Trans. Graph. **31**(6), Article 139. (2012)
73. Levin, A., Weiss, Y., Durand, F., Freeman, W.T.: Understanding blind deconvolution algorithms. IEEE Trans. Pattern Anal. Mach. Intell. **33**(12), 2354–2367 (2011)
74. Chan, S.H., Wang, X., Elgendy, O.A.: Plug-and-play ADMM for image restoration: fixed point convergence and application. In: IEEE Trans. Comput. Imaging, (In press). ArXiv: https://arxiv.org/abs/1605.01710. (2016)
75. Zhao, N., Wei, Q., Basarab, A., Kouame, D., Toureneret, J.Y.: Fast single image super-resolution using a new analytical solution for L_2–L_2 problems. http://arXiv.org/abs/1510.00143v3. (2016)
76. Dabov, K., Foi, A., Katkovnik, V., Egiazarian, K.: Image denoising by sparse 3D transform-domain collaborative filtering. IEEE Trans. Image Process. **16**(8), 2080–2095 (2007)
77. Schuler, C., Hirsch, M., Harmeling, S., Scholkopf, B.: Learning to Deblur. IEEE Trans. Pattern Anal. Mach. Intell. **38**(7), 1439–1451 (2016)
78. Nguyen, K., Fookes, C., Sridharan, S., Tistarelli, M., Nixon, M.: Super-resolution for biometrics: a comprehensive survey. Pattern Recognit. **78**, 23–42 (2018)
79. Wei, X., Li, Y., Shen, H., Xiang, W., Murphey, Y.: Joint learning sparsifying linear transformation for low-resolution image synthesis and recognition. Pattern Recognit. **66**, 412–424 (2018)
80. Wang, L., Huang, Z., Gong, Y., Pan, C.: Ensemble based deep networks for image super-resolution. Pattern Recognit. **68**, 191–198 (2017)
81. Kumar, N., Verma, R., Sethi, A.: Convolutional neural networks for wavelet domain super resolution. Pattern Recognit. Lett. **90**, 65–71 (2017)
82. Jebadurai, J., Peter, J.D.: SK-SVR: sigmoid kernel support vector regression based in-scale single image super-resolution. Pattern Recognit. Lett. **94**, 144–153 (2017)
83. Kwon, Y., Kim, K.I., Tompkin, J., et al.: Efficient learning of image super-resolution and compression artifact removal with semi-local Gaussian processes. IEEE Trans. Pattern Anal. Mach. Intell. **37**(9), 1792–1805 (2015)
84. Polatkan, G., Zhou, M., Carin, L.L., et al.: A Bayesian nonparametric approach to image super-resolution. IEEE Trans. Pattern Anal. Mach. Intell. **37**(2), 346–358 (2015)
85. Khare, V., Shivakumara, P., Raveendran, P., Blumenstein, M.: A blind deconvolution model for scene text detection and recognition in video. Pattern Recognit. **54**, 128–148 (2016)
86. Li, W., Chen, D., Lv, Z., Yan, Y., Cosker, D.: Learn to model blurry motion via directional similarity and filtering. Pattern Recognit. **75**, 327–338 (2018)
87. Pan, J., Sun, D., Pfister, H., Yang, M.H.: Deblurring image via dark channel prior. IEEE Trans. Pattern Anal. Mach. Intell. (2017). https://doi.org/10.1109/tpami.2017.275380
88. Zhang, H., Wipf, D., Zhang, Y.: Multi-observation blind deconvolution with an adaptive sparse prior. IEEE Trans. Pattern Anal. Mach. Intell. **36**(8), 1628–1643 (2014)
89. Tai, Y.W., Chen, X., Kim, S., et al.: Nonlinear camera response functions and image deblurring: theoretical analysis and practice. IEEE Trans. Pattern Anal. Mach. Intell. **35**(10), 2498–2512 (2013)
90. Kupyn, O., Budzan, V., Mykhailych, M., Mishkin, D., Matas, J.: DeblurGAN: blind motion deblurring using conditional adversarial networks. https://arXiv.org/abs/1711.07064v2. (2018)
91. Nah, S., Kim, T.H., Lee, K.M.: Deep multi-scale convolutional neural network for dynamic scene deblurring. In: 2017 IEEE Conference on Computer Vision and Pattern Recognition (CVPR), Honolulu, pp. 257–265. (2017)
92. Nimisha, T.M., Singh, A.K., Rajagopalan, A.N.: Blur-invariant deep learning for blind-deblurring. In: 2017 IEEE International Conference on Computer Vision (ICCV), Venice, pp. 4762–4770. (2018)
93. Zhou, E., Fan, H., Cao, Z., Jiang, Y., Yin, Q.: Learning face hallucination in the wild. In: Proceedings of the Twenty-Ninth AAAI Conference on Artificial Intelligence, (2015)
94. Xu, X., Sun, D., Pan, J., Zhang, Y., Pfister, H., Yang, M.: Learning to super-resolve blurry face and text images. In: 2017 IEEE International Conference on Computer Vision (ICCV), Venice, pp. 251–260. (2018)
95. Feng, N., Wang, J., Wang, W.: Sparse signal recovery with prior information by iterative reweighted least squares algorithm. J. Inverse Ill-posed Problems **36**(2), 171–184 (2017)
96. Lu, C., Lin, Z., Yan, S.: Smoothed low rank and sparse matrix recovery by iteratively reweighted least squares minimization. IEEE Trans. Image Process. **24**(2), 646–654 (2015)
97. Zhang, K., Zuo, W., Gu, S., Zhang, L.: Learning deep CNN denoiser prior for image restoration. In: 2017 IEEE Conference on Computer Vision and Pattern Recognition (CVPR), pp. 2808–2817 (2017)

Wen-Ze Shao received the BS degree in Science of Information and Computation in June 2003 and the Ph.D. degree in Pattern Recognition and Intelligent System in July 2008, both from Nanjing University of Science and Technology, Nanjing, China. From June 2003 to December 2011, he served as an officer in the People's Liberation Army of China. In January 2012, he joined Nanjing University of Posts and Telecommunications as an Assistant Professor. From May 2014 to June 2015, he also worked as a Post doc Researcher at Department of Computer Science in Technion—Israel Institute of Technology. He is currently an Associate Professor in Nanjing University of Posts and Telecommunications, working in the fields of computational imaging and computer vision harnessing both variational and learning-based methods.

Qi Ge received the BS degree in Science of Information and Computation in 2006 and the MS degree in Applied Mathematics in 2009, both from Nanjing University of Information and Engineering, Nanjing, China, and the Ph.D. degree in Pattern Recognition and Intelligent System in 2013 from Nanjing University of Science and Technology, Nanjing, China. Now, she serves as an Assistant Professor at College of Telecommunications and Information Engineering in Nanjing University of Posts and Telecommunications. She is particularly interested in the fields of variational PDE approaches, probabilistic graphical models, sparse representation and their applications to image restoration, segmentation and so on.

Li-Qian Wang received the BS degree in Science of Information and Computation in June 2006, the MS degree in Computer Application Technology in 2008 and the Ph.D. degree in Pattern Recognition and Intelligent System in 2015, all from Nanjing University of Science and Technology, Nanjing, China. She is currently an Assistant Professor at College of Telecommunications and Information Engineering in Nanjing University of Posts and Telecommunications. Her research interests include variational partial differential equations with applications in image processing, image restoration, image enhancement and pattern recognition.

Yun-Zhi Lin received the BE degree in Automation in June 2018 from Southeast University, Nanjing, China. From September to December 2017, he was sponsored by National Undergraduate Exchange Scholarship of China working as a research assistant at Applied Nonlinear Control Laboratory in University of Alberta, Canada. Since August 2018, he has started his new life as a graduate student in School of Electrical and Computer Engineering at Georgia Institute of Technology, GA, USA. His research interests include computer graphics, computer vision and robotics. Now he mainly focuses on the field of robotics simulation and some other related topics.

Hai-Song Deng received the BS degree in Mathematics in 2003 from Xuzhou Normal University, Xuzhou, China, the MS degree in Statistics in 2006 and the Ph.D. degree in Management Science and Engineering in 2011 both from Nanjing University of Science and Technology, Nanjing, China. In July 2011, she joined Nanjing Audit University as an Assistant Professor. Now, she is an Associate Professor at School of Statistics and Mathematics in Nanjing Audit University. Her research fields include Bayesian statistics, sparse optimization, surrogate modeling, design and analysis of computer experiments.

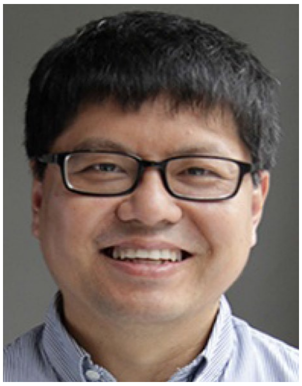

Hai-Bo Li received the BE degree in Wireless Engineering in 1985 and the MS degree in Communication and Electronic Systems in 1988, both from Nanjing University of Posts and Telecommunications, Nanjing, China, and the Ph.D. degree in Information Theory in 1993 from Lin ping University, Sweden. In 1997, he became docent (UK equivalent senior lecturer, US equivalent associate professor) in image coding, and in 1999, he became the youngest lifetime professor of signal processing in Umea University, Sweden. Now, he is a Professor of Innovative Media Technology in KTH Royal Institute of Technology. His research interest is mainly media signal processing, including image coding, video compression, motion estimation, facial and hand gesture recognition for the next generation of mobile phones, invisible interaction technology and so on.